Title

Large-Area Plasmonic Photoconductive Nanoantenna Arrays for Terahertz Wave Generation and Detection in High-Performance Time-Domain Terahertz Systems

Author

Yardimci, Nezih Tolga

Publication Date

2017

Peer reviewed|Thesis/dissertation

University of California
Los Angeles

Large-Area Plasmonic Photoconductive Nanoantenna Arrays for Terahertz Wave Generation and Detection in High-Performance Time-Domain Terahertz Systems

A dissertation submitted in partial satisfaction
of the requirements for the degree
Doctor of Philosophy in Electrical Engineering

by

Nezih Tolga Yardimci

2017

ABSTRACT OF THE DISSERTATION

Large-Area Plasmonic Photoconductive Nanoantenna Arrays for Terahertz Wave Generation and Detection in High-Performance Time-Domain Terahertz Systems

by

Nezih Tolga Yardimci

Doctor of Philosophy in Electrical Engineering

University of California, Los Angeles, 2017

Professor Mona Jarrahi, Chair

Time-domain terahertz imaging and spectroscopy systems have unique functionalities for chemical identification, material characterization, biological sensing, medical imaging, and security screening. Photoconductive sources and detectors are commonly used for the generation and detection of terahertz pulses in compact time-domain terahertz systems operating at room temperature. However, the low radiation power of conventional photoconductive sources and the low responsivity of conventional photoconductive detectors have limited the scope of the potential uses of these systems. To improve the performance of time-domain terahertz systems, photoconductive sources and detectors consisting of large-area plasmonic nanoantenna arrays are designed, fabricated and experimentally characterized.

To increase the radiation power of photoconductive sources, the plasmonic nanoantenna arrays are designed to enhance the absorption of optical pump photons near them. The enhanced optical absorption leads to stronger ultrafast photocurrent levels coupled to the nanoantenna arrays. The

nanoantenna arrays are designed to serve as broadband terahertz radiating elements. Hence, high-power and broadband pulsed terahertz radiation is generated. Higher terahertz radiation powers and device efficiencies are achieved by a tighter optical pump confinement enabled by plasmonic nanocavities formed near the plasmonic nanoantenna arrays. Record-high terahertz radiation powers as high as 4 mW are achieved over a 0.1 – 5 THz frequency range.

To increase the responsivity of photoconductive detectors, the plasmonic nanoantenna arrays are designed to maximize the interaction between the optical pump photons and the incident terahertz radiation at the nanoscale. The impact of the nanoantenna geometry on terahertz detection responsivity and bandwidth is analyzed theoretically and experimentally. By optimizing the geometry of the nanoantenna arrays, broadband time-domain terahertz spectroscopy with a record-high dynamic range of 107 dB is demonstrated.

The dissertation of Nezih Tolga Yardimci is approved.

Pietro Musumeci

Chee-Wei Wong

Benjamin S. Williams

Mona Jarrahi, Committee Chair

University of California, Los Angeles

2017

To my family

Table of Contents

CHAPTER 1: Introduction 1

1.1 Terahertz Science and Technology 1

1.2 Time-Domain Terahertz Systems 2

1.3 Pulsed Terahertz Generation 4

1.3.1 Pulsed Terahertz Generation through Nonlinear Crystals 4

1.3.2 Pulsed Terahertz Generation through Photoconductive Sources 5

1.4 Pulsed Terahertz Detection 9

1.4.1 Electro-optic Pulsed Terahertz Detection 9

1.4.2 Pulsed Terahertz Detection through Photoconductive Detectors 11

1.5 Plasmonic Photoconductive Terahertz Sources and Detectors 12

1.6 Outline of the Dissertation 13

Chapter 2: Terahertz Generation through Large-Area Plasmonic Nanoantenna Arrays 14

2.1. Overview 14

2.2. Sources Fabricated on Semi-Insulating GaAs Substrate 14

2.2.1 Source Design 14

2.2.2 Source Fabrication 17

2.2.3 Source Characterization and Analysis 18

2.3. Sources Fabricated on Short-Carrier-Lifetime Substrates 22

2.3.1 Material Growth 23
2.3.2 Source Design and Fabrication 25
2.3.3 Source Characterization and Analysis 26
2.4. Plasmonic Nanocavity Sources 33
2.4.1 Source Design and Fabrication 34
2.4.2 Source Characterization 39
2.5. Telecommunication-Compatible Sources 46
2.5.1. Source Design 47
2.5.2. Source Fabrication and Characterization 49
Chapter 3: Terahertz Detection through Large-Area Plasmonic Nanoantenna Arrays 54
3.1. Overview 54
3.2. Detector Design 55
3.3. Detector Fabrication 60
3.4. Detector Characterization 61
Chapter 4: Conclusion and Future Directions 67
References 69

LIST OF FIGURES AND TABLES

Figure 1.1. The electromagnetic spectrum from radio waves to gamma rays.

Figure 1.2. A time-domain terahertz spectroscopy setup with a delay stage and photoconductive source and detector.

Figure 1.3. A conventional large-area photoconductive terahertz source.

Figure 1.4. A time-domain terahertz spectroscopy setup with electro-optic detection.

Figure 2.1. Schematic diagram and operation principle of the large area plasmonic nanoantenna array fabricated on SI-GaAs substrate.

Figure 2.2. Power transmission of a TM-polarized optical beam into the SI-GaAs substrate as a function of optical wavelength. Inset shows color plot of optical absorption in the SI-GaAs substrate in response to a TM-polarized optical beam at 800 nm optical wavelength.

Fig. 2.3. The SEM image of a fabricated large-area plasmonic nanoantenna array with 5 μm long plasmonic nanoantennas, (b) SEM image of the plasmonic nanoantennas.

Figure 2.4. Photocurrent and radiated power for the large-area plasmonic nanoantenna arrays with 5 μm and 10 μm nanoantenna lengths fabricated on SI-GaAs substrate.

Figure 2.5. Radiated electric field in the time domain and radiated power in the frequency domain for the large area plasmonic photoconductive sources with 5 μm and 10 μm plasmonic grating lengths fabricated on SI-GaAs substrate.

Table 2.1. Carrier lifetime of the grown LT-GaAs, ErAs:GaAs, and LuAs:GaAs compounds.

Figure 2.6. (a) Schematic diagram and operation concept of the fabricated large-area plasmonic photoconductive nanoantenna array sources. (b) Optical microscope and scanning electron microscope (SEM) images of a fabricated large-area plasmonic photoconductive nanoantenna array source prototype.

Figure 2.7. Measured dark current and photocurrent levels of the large-area plasmonic photoconductive nanoantenna arrays fabricated on the LT-GaAs and ErAs:GaAs substrates are shown in (a) and (b), respectively. Measured dark current and photocurrent levels of large-area plasmonic photoconductive nanoantenna arrays fabricated on the LT-GaAs and LuAs:GaAs substrates are shown in (c) and (d), respectively. Photocurrent levels are measured at 800 mW optical pump power.

Figure 2.8. (a) Measured terahertz power levels at 800 mW optical pump power for the large-area plasmonic photoconductive nanoantenna arrays fabricated on the LT-GaAs and ErAs:GaAs substrates. (b) Measured terahertz power levels at 800 mW optical pump power for the large-area plasmonic photoconductive nanoantenna arrays fabricated on the LT-GaAs and LuAs:GaAs substrates.

Figure 2.9. (a) Radiated electric field in the time domain from the large area plasmonic photoconductive sources fabricated on the LT-GaAs and ErAs:GaAs substrates. (b) Radiated electric field in the time domain from the large area plasmonic photoconductive sources fabricated on the LT-GaAs and LuAs:GaAs substrates.

Figure 2.10. (a) Radiated spectra from the large area plasmonic photoconductive sources fabricated on the LT-GaAs and ErAs:GaAs substrates. (b) Radiated spectra from the large area plasmonic photoconductive sources fabricated on the LT-GaAs and LuAs:GaAs substrates.

Figure 2.11. Schematic diagram and operation principle of the presented photoconductive source based on a nanocavity formed by a plasmonic nanoantenna array and DBR structure.

Figure 2.12. (a) The reflectivity of the designed plasmonic nanoantennas and the optical absorption in the top GaAs region as a function of the wavelength. (b) Two-dimensional color plot of the optical absorption in the top GaAs region at a wavelength of 775 nm.

Figure 2.13. Optical microscopy image of the terahertz source prototype and scanning electron microscopy images of the bias lines, shadow metals and plasmonic nanoantennas.

Figure 2.14. (a) The estimated and measured optical reflectivities of the plasmonic nanoantennas as a function of the wavelength. (b) The estimated optical absorption in the top GaAs layer and the measured photocurrent in the terahertz source prototype.

Figure 2.15. (a) Photocurrents in the nanocavity-based terahertz source and the terahertz source fabricated on the LT-GaAs substrate as a function of the bias voltage under an optical pump power of 720 mW. (b) Photocurrents in the nanocavity-based terahertz source and the terahertz source fabricated on the LT-GaAs substrate as a function of the optical pump power under a bias voltage of 18 V.

Figure 2.16. (a) Radiated terahertz power levels of the nanocavity-based terahertz source and the terahertz source fabricated on the LT-GaAs substrate as a function of the bias voltage under an optical pump power of 720 mW. (b) Radiated terahertz power levels of the nanocavity-based terahertz source and the terahertz source fabricated on the LT-GaAs substrate as a function of the optical pump power under a bias voltage of 18 V.

Figure 2.17. (a) The radiated electric fields and (b) the corresponding radiated power spectra of the nanocavity-based terahertz source and the terahertz source fabricated on the LT-GaAs substrate.

Figure 2.18. Schematic diagram of the presented photoconductive terahertz source based on a large-area plasmonic nanoantenna array fabricated on an ErAs:InGaAs substrate.

Figure 2.19. Optical transmission spectrum through the plasmonic nanoantennas into the ErAs:InGaAs substrate, inset shows optical absorption inside the ErAs:InGaAs substrate at 1550 nm pump wavelength.

Figure 2.20. Optical microscope image of the plasmonic terahertz source and scanning electron microscope image of the plasmonic nanoantennas are shown in (a) and (b), respectively.

Figure 2.21. (a) The induced photocurrent and (b) terahertz radiation power from a large area plasmonic photoconductive source prototype as a function of the optical pump power and bias voltage.

Figure 2.22. The radiated electric field in the time domain and radiated power in the frequency domain are shown in (a) and (b), respectively.

Figure 3.1. Schematic diagram of plasmonic photoconductive nanoantenna arrays used for detecting pulsed terahertz radiation.

Figure 3.2. (a) Optical transmission spectrum through the plasmonic nanoantennas, inset shows optical absorption inside the substrate at a vertical cross-section of the nanoantennas at 800 nm pump wavelength. (b) Optical absorption between the nanoantenna tips at a 10 nm depth inside

the substrate, the inset color plots show optical absorption profile within a 150 nm depth inside the substrate.

Figure 3.3. (a) Electric field enhancement factor in the middle of the nanoantenna tips as a function of the nanoantenna length and tip-to-tip gap size is shown in (a) and (b), respectively. Electric field enhancement factor between the nanoantenna tips at 1 THz as a function of the nanoantenna length and tip-to-tip gap size is shown in (c) and (d), respectively.

Figure 3.4. Scanning electron microscope image of a plasmonic nanoantenna array fabricated on a LT-GaAs substrate with a nanoantenna length of 2 μm and tip-to-tip gap size of 500 nm.

Figure 3.5. The measured photocurrent of a detector prototype with a nanoantenna length of 4 μm and tip-to-tip gap size of 500 nm in the time-domain and the corresponding power spectra are shown in (a) and (b), respectively. (c) Responsivity of detector prototypes with nanoantenna lengths of 2 μm and 4 μm and a tip-to-tip gap size of 500 nm at 1 THz, (d) responsivity of detector prototypes with a nanoantenna length of 2 μm and nanoantenna tip-to-tip gap sizes of 250 nm, 500 nm, and 1 μm at 1 THz.

Figure 3.6. (a) The measured noise current of the detector prototypes with nanoantenna lengths of 2 μm and 4 μm and a tip-to-tip gap size of 500 nm, (b) the measured noise current of the detector prototypes with a nanoantenna length of 2 μm and nanoantenna tip-to-tip gap sizes of 250 nm, 500 nm, and 1 μm, (c) the measured SNR of the detector prototypes with nanoantenna lengths of 2 μm and 4 μm and a tip-to-tip gap size of 500 nm, (d) the measured SNR of the detector prototypes with a nanoantenna length of 2 μm and nanoantenna tip-to-tip gap sizes of 250 nm, 500 nm, and 1 μm.

Figure 3.7. The measured power spectrum by the detector prototype with a nanoantenna length of 4 μm and a tip-to-tip gap size of 500 nm relative to the measured noise power at 170 mW optical pump power. The presented data are achieved by capturing and averaging 750 photocurrent data points with an integration time of 10 ms.

ACKNOWLEDGMENTS

First, I would like to express my special appreciation and gratitude to my advisor, Professor Mona Jarrahi for giving me the opportunity to work on this innovative project. Her patience, time, and support have made the steps I took for my research much easier. She has also been the perfect role model, showing me how to be an innovative, self-motivated and dedicated scientist.

Second, I would like to thank my committee members; Professor Chee-Wei Wong, Professor Benjamin S. Williams, and Professor Pietro Musumeci for their valuable comments and suggestions on my research. I also want to thank my collaborators; Professor Seth Bank and Dr. Rodrigo Salas at University of Texas Austin and Professor Hong Lu at Nanjing University for growing unique semiconductor substrates that I used for my research. I would also like to send my special gratitude to Professor F. Levent Degertekin at Georgia Institute of Technology to give me a chance to experience the graduate life by offering me a summer internship in his research group much before my graduate studies started. With this opportunity, I obtained my initial passion for research and decided to pursue a Ph.D. degree.

I would also like to thank Prof. Shang-Hua Yang for his invaluable suggestions and guidance throughout my graduate studies. I would like to thank all current and former members of Terahertz Electronics Laboratory, namely, Dr. Semih Cakmakyapan, Dr. Ning Wang, Dr. Christopher Berry, Deniz Turan, Steve Lu, Leihao Wei, Yen-Ju Lin, Xurong Li, and Soroosh Hemmati, for their contributions to my research.

Finally, I would like to express my gratitude to my family; my fiancée, my parents and my brother. Their love and support are the main sources of my motivation.

VITA

2007 – 2012	B.S. in Electrical and Electonics Engineering, Middle East Technical University.
2011	Visiting Scholar under Professor F. Levent Degertekin, Georgia Institute of Technology.
2012 – 2014	M.S. in Electrical Engineering, University of Michigan – Ann Arbor.
2012 – 2014	Graduate Student Researcher under Professor Mona Jarrahi, University of Michigan – Ann Arbor.
2014 – 2017	Graduate Student Research Assistant under Professor Mona Jarrahi, University of California – Los Angeles.

Selected Journal Papers and Conference Proceedings

- N. T. Yardimci, M. Jarrahi, "High sensitivity terahertz detection through plasmonic nanoantenna arrays," *Nature Scientific Reports*, 7, 42667, 2017.
- N. T. Yardimci, M. Jarrahi, "High power telecommunication-compatible photoconductive terahertz sources based on plasmonic nanoantenna arrays," *Applied Physics Letters*, 109, 2016
- N. T. Yardimci, R. Salas, Erica M. Krivoy, Hari P. Nair, S. R. Bank, M. Jarrahi, "Impact of Substrate Characteristics on Performance of Large Area Plasmonic Photoconductive Sources," *Optics Express*, 23, 32035-32043, 2015

- N. T. Yardimci, S.-H. Yang, C. W. Berry, M. Jarrahi, "High Power Terahertz Generation Using Large Area Plasmonic Photoconductive Sources", *IEEE Transactions on Terahertz Science and Technology*, 5, 223-229, 2015.

- N. T. Yardimci, M. Jarrahi, "Plasmonic Nanoantenna Arrays for High-Sensitivity and Broadband Terahertz Detection", *Proc. IEEE International Antennas and Propagation Symposium*, San Diego, CA, July 9-14, 2017. (Honorable Mention)

- N. T. Yardimci, M. Jarrahi, "Telecommunication Compatible Terahertz Sources based on Plasmonic Nanoantenna Arrays", *Proc. IEEE International Antennas and Propagation Symposium*, Fajardo, Puerto Rico, June 26 - July 1, 2016. (Honorable mention).

- N. T. Yardimci, M. Jarrahi, "High-Power, Broadband Terahertz Radiation from Large Area Plasmonic Photoconductive Sources Operating at Telecommunication Optical Wavelengths", *IEEE Microwave Symposium Digest*, San Francisco, CA, May 22-27, 2016. (Best Student Paper Competition Finalist)

- N. T. Yardimci, S.-H. Yang, M. Jarrahi, "High Power Pulsed Terahertz Radiation From Large Area Photoconductive Sources", *Proc. International Conference on Infrared, Millimeter and Terahertz Waves*, Hong Kong, August 23-28 2015. (Invited talk), (Best Student Paper Award - 3rd place)

- N. T. Yardimci, M. Jarrahi, "3.8 mW Terahertz Radiation Generation through Plasmonic Nanoantenna Arrays", *Proc. IEEE International Antennas and Propagation Symposium*, Vancouver, BC, Canada, July 19-25, 2015. (Best Student Paper Competition Finalist)

CHAPTER 1: Introduction

1.1 Terahertz Science and Technology

The final frontier of the electromagnetic spectrum, the terahertz band, lies between the microwave region and the infrared region. Without any strict border, it is assumed that this band covers the electromagnetic spectrum from 0.1 THz to 10 THz, as shown in Figure 1.1. This frequency range had been called the "terahertz gap" for a long time due to the technological limitations of devices that can operate at these frequencies. Recent advances in terahertz science and technology have been closing the gap quite rapidly for the last several decades and have made terahertz frequencies available for people to use in many exciting applications [1-3].

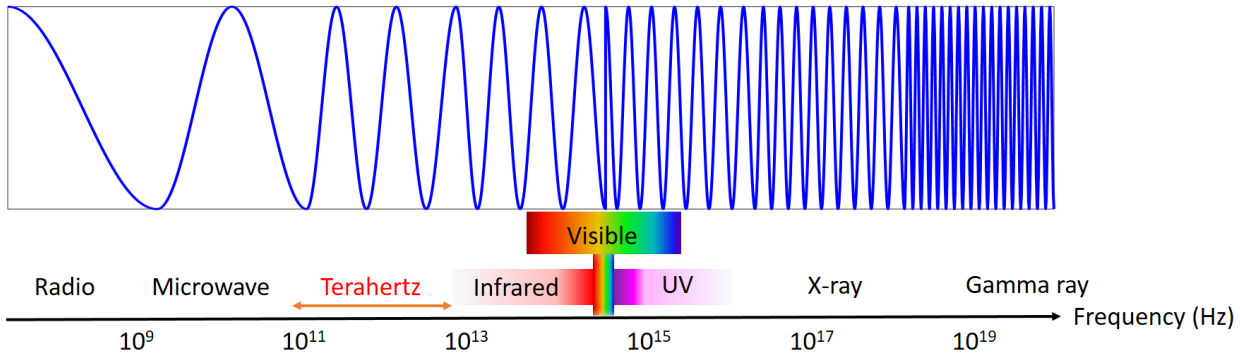

Figure 1.1. The electromagnetic spectrum from radio waves to gamma rays.

The fact that terahertz radiation can probe low energy light-matter interactions makes this band very appealing for researchers [4]. These interactions include phonons in solids, the rotational transition of molecules and the vibrational modes of large molecules. Terahertz waves can be used to characterize or identify many materials such as solid crystals, gases, polar liquids, and composites, which makes this band applicable for biosensing [5], chemical identification [6] and

material characterization applications [7]. The energy of photons at terahertz frequencies is non-ionizing and non-destructive. Therefore, terahertz waves offer many promising and unique applications in biomedical imaging [8] and non-destructive evaluation [9]. Most of the materials that are opaque in the visible region of the electromagnetic spectrum are much more transparent at terahertz frequencies. Thus, terahertz waves can also be used for security screening applications [10].

Two types of measurement can be performed for imaging or spectroscopy purposes with terahertz waves: frequency-domain measurement and time-domain measurement. Continuous-wave (CW) terahertz sources and detectors are used for frequency-domain measurements. The experimental setup is very simple for this type of measurement. The generated terahertz power from the CW source is directly detected by the detector [11]. By placing a sample between the source and the detector, the transmission of the wave through the sample can be understood. By using frequency-tunable CW terahertz sources and detectors [12], frequency-domain spectroscopy can be performed. Since the focus of this study is high-performance terahertz sources and detectors that can be used in time-domain terahertz systems, the details of frequency-domain setups are not discussed here.

1.2 Time-Domain Terahertz Systems

In time-domain measurements, a terahertz source generates narrow pulses. These pulses in the time domain correspond to a broad signal that covers the frequencies of the terahertz band in the frequency domain. The generated pulses are detected in the time-domain. However, because there is no measurement unit that can offer a sub-picosecond sampling rate, a pump-probe

technique is used to obtain the terahertz pulses. This makes time-domain terahertz systems more complex than frequency-domain systems.

A common time-domain terahertz setup is shown in Figure 1.2. A femtosecond laser is used to generate ultrashort femtosecond pulses at near-infrared wavelengths. This optical beam is split into two parts. One part, the pump line, pumps the terahertz source, which can be a nonlinear crystal or a photoconductive antenna. A terahertz pulse is generated by the source. The generated pulse can be focused on the terahertz detector by using various terahertz optics. The other part of the optical beam, the probe line, goes through a delay stage and focuses on the terahertz detector, which can also be a nonlinear crystal or a photoconductive antenna. As the position of the delay line changes, the timing between the incident terahertz pulse and the optical beam on the terahertz detector changes. Therefore, the incident terahertz field can be sampled by obtaining the response of the detector at different delay stage positions. A more detailed discussion of the physics of pulsed terahertz sources and detectors is given in Sections 1.3 and 1.4.

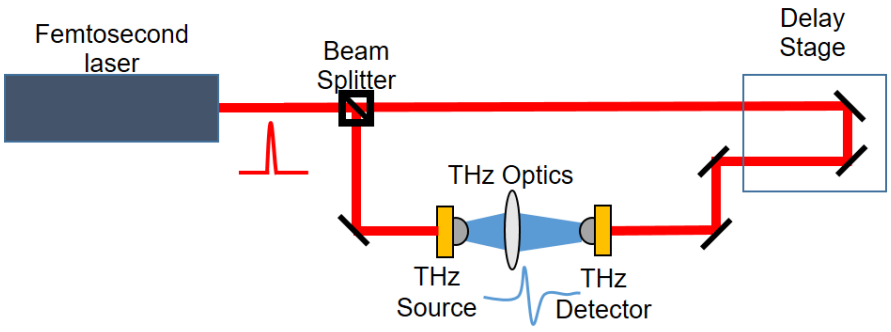

Figure 1.2. A time-domain terahertz spectroscopy setup with a delay stage and photoconductive source and detector.

A sample can be placed between the source and detector, and its response to the incident terahertz field can be obtained. Spectral information of the sample can be obtained by taking the

Fourier transform of the time-domain data. The most important advantage of time-domain measurements is that the incident electric field rather than the power is detected. Therefore, both phase and amplitude information can be acquired at the same time. This means that with time-domain measurements, all of the optical parameters of the sample being tested can be acquired. This unique specification of time-domain measurements opens the door for exciting spectroscopy, hyperspectral imaging and thickness measurement applications [13-15]. However, the functionalities of these systems are limited by the performance of terahertz sources and detectors. The size and cost of time-domain terahertz systems are other concerns that should be considered when choosing the right source and detector for the time-domain measurement system.

1.3 Pulsed Terahertz Generation

For a time-domain terahertz imaging or spectroscopy system with a high dynamic range over a broad frequency range, high-power and broadband terahertz pulses must be generated. The insufficient radiation power level and narrow bandwidth of the available terahertz sources limit the performance of time-domain systems very significantly. There are various ways to generate pulsed terahertz radiation. The most popular means for optical-to-terahertz conversion are nonlinear crystals and photoconductive sources. Since the dissertation is about photoconductive devices, a more-detailed sub-section is provided for photoconductive sources.

1.3.1 Pulsed Terahertz Generation through Nonlinear Crystals

Nonlinear crystals generate the terahertz pulses by optical rectification, which is basically a difference frequency generation process. For this reason, the crystals that are used for this application are chosen to have large second-order susceptibility. There have been efforts to use

periodically poled structures or to tilt the phase-front of the optical pump with regards to the propagation direction of terahertz pulses to improve the phase matching between optical and terahertz pulses [16, 17]. The goal is to increase the length of optical interaction with the nonlinear crystal as much as possible, but the material absorption eventually puts a limit on the efficient field interaction length. Optical-to-terahertz conversion efficiency when using nonlinear crystals is limited by the Manley-Rowe rule [18]. This means that one optical pump photon can only generate one terahertz photon. Therefore, the optical-to-terahertz conversion efficiency is inherently limited by the energy ratio between an optical photon and terahertz photon. It is common to generate high-energy terahertz pulses through nonlinear optical processes using high energy laser pulses with low repetition rates [19]. However, these lasers are bulky and expensive compared to compact femtosecond lasers, which have high repetition rates. To increase efficiency and not burn the crystal, the crystal is usually cooled down to cryogenic temperatures. Measurement speed is another drawback of time-domain terahertz systems with low-repetition-rate lasers. These reasons prevent the utilization of nonlinear crystals in compact time-domain terahertz systems with high dynamic ranges.

1.3.2 Pulsed Terahertz Generation through Photoconductive Sources

Photoconductive terahertz sources are the most common sources of pulsed terahertz radiation in compact time-domain terahertz imaging and spectroscopy systems [20, 21]. A photoconductive source consists of a terahertz antenna fabricated on a photoconductive semiconductor substrate. The terahertz antenna is designed to operate at terahertz frequencies. The type of antenna can be chosen based on the needs of the specific application. A spiral or bowtie antenna can be used for

broadband signal generation. When the active region, which is the region between the antenna electrodes, is illuminated by the optical pump pulse, electron-hole pairs are generated in the semiconductor. If an external bias voltage is applied from the antenna electrodes, the photo-generated carriers drift to the corresponding contact electrodes, and an ultrafast photocurrent is induced within the device. As this photocurrent drives the antenna, a pulsed radiation is generated. A silicon lens is generally used to collimate the generated beam and couple it to air more efficiently.

The generated pulse consists of different frequency components in a broad frequency range. For terahertz applications, it is desired to have all frequency components in the terahertz region. However, only the carriers that are generated in very close proximity to the antenna electrodes can drift to the contact electrodes in a very short time-scale and contribute to the terahertz frequencies of the radiated pulse. In fact, if we consider using a GaAs substrate as the photoconductive semiconductor, only the carriers that are generated within 200-300 nm from the contact electrode can contribute to the frequency components in the terahertz region. The rest of the photo-generated carriers add low-frequency components to the generated pulse. These frequency components do not have any importance in terahertz measurements but cause an increase in photocurrent and thermal power dissipation. This results in early thermal breakdowns for photoconductive terahertz sources.

A common solution to this problem is to use short-carrier-lifetime semiconductors as photoconductors [22, 23]. The carrier lifetime of these semiconductors is typically less than a picosecond. By using these semiconductors, the carriers that are generated a few hundred nanometers away from the antenna can still drift to the electrodes. However, slow carriers that do not contribute to the terahertz frequencies of the radiation recombine inside the semiconductor

before reaching the electrodes. Therefore, they do not increase the photocurrent and thermal dissipation unnecessarily. Consequently, the photoconductive sources can be pumped with a higher-power optical pump, and stronger terahertz fields are generated. The problem for conventional photoconductive sources that are fabricated on short-carrier-lifetime semiconductors is the low optical-to-terahertz conversion efficiency. Only a very small portion of the photo-generated carriers can contribute to terahertz radiation and the carrier mobility is degraded due to the semiconductor defects.

Another photoconductive source design, which is one of the inspirational points for the study in this dissertation, is large-area photoconductive sources. These devices offer an antenna-less solution to generate pulsed terahertz radiation. They are very promising candidates for time-domain terahertz imaging and spectroscopy systems since they offer relatively high power and broadband terahertz radiation [25-27]. Figure 1.3 shows a schematic diagram of a large-area source. The device consists of interdigitated metal bias lines deposited on a photoconductive semiconductor. When the source is illuminated by an optical pump beam, photo-generated electrons and holes are accelerated in opposite directions by the external bias electric field applied from the bias lines. Rather than using a separate antenna, each electron-hole pair is considered an elementary Hertzian dipole. The acceleration and separation of photo-carriers induce a time-varying dipole moment within the device active area, which generates terahertz radiation. The radiation resistance of such a dipole cannot be comparable with that of a dipole induced by metal antennas. However, the number of these elementary dipoles can be so high that the total radiated field can eventually be stronger than the conventional photoconductive antennas. The reason why large-area photoconductive sources can offer high power terahertz radiation is their capacity to handle relatively high optical power without suffering from the

carrier screening effect and thermal breakdown. The optical beam spot size is adjusted to illuminate the whole area of the device. Therefore, the intensity of the light on the device can be reduced. Additionally, the capability of large-area photoconductive sources in offering broadband terahertz radiation is because terahertz radiation is generated by time-varying dipole moments induced within the device active area with dipole lengths much smaller than terahertz wavelength. A dielectric antireflection coating layer is usually used to increase the optical transmission to the substrate. Every second gap between anode and cathode electrodes is shadowed to cause the opposite direction photocurrent to vanish. This current would generate a radiation that would destructively interfere with the pulse generated from the main gaps.

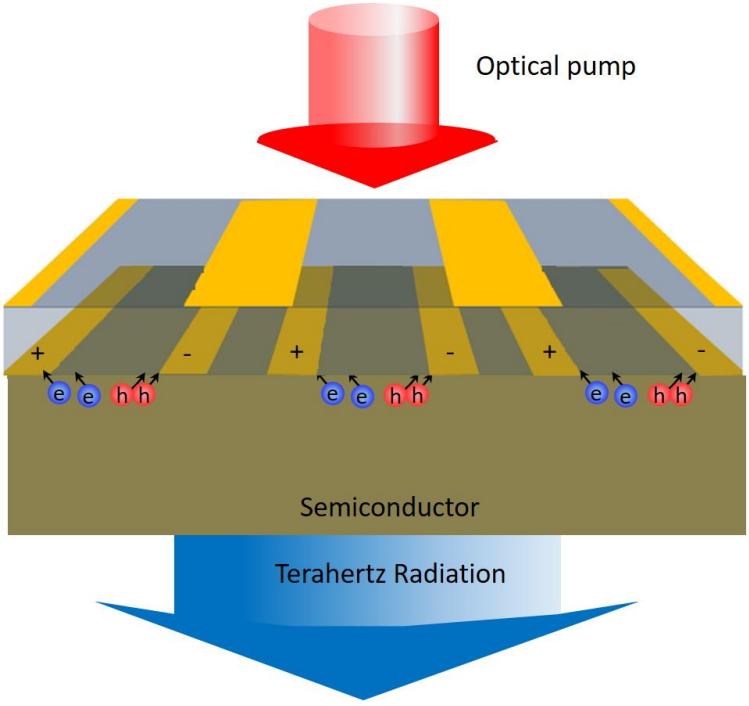

Figure 1.3. A conventional large-area photoconductive terahertz source.

Radiated power level of 1.5 mW has been achieved by the use of large-area photoconductive sources at 750 mW optical pump power with 250 kHz repetition rate [26]. This proves that

despite their great promise for generating high-power pulsed terahertz radiation by accommodating higher optical pump power levels, the optical-to-terahertz conversion efficiency of conventional large area photoconductive emitters is limited by the weak effective dipole moment induced within the device active area. This is mainly because of the carrier scattering inside the semiconductor substrate, which limits the carrier acceleration and transport velocity.

1.4 Pulsed Terahertz Detection

The detector performance is as important as the source performance for time-domain systems to offer a high dynamic range and broadband operation. High sensitivity and broad detection bandwidth are required specifications for terahertz detectors. The two common pulsed terahertz detection techniques are electro-optic detection and detection through photoconductive devices.

1.4.1 Electro-optic Pulsed Terahertz Detection

Nonlinear crystals are used for the electro-optic detection of terahertz waves. The radiation is sensed by Pockels effect [28, 29]. In other words, the birefringent aspect of the crystal varies as the electric field incident on it changes. Therefore, when the terahertz beam is incident on the nonlinear crystal, the refractive indices of the crystal on different axes will vary as a direct function of the strength of the terahertz field applied. The polarization of the probe beam, which is also incident on the nonlinear crystal, changes as the refractive indices vary. As shown in Figure 1.4, the change in the polarization of the optical beam can be sensed by using a polarizing beam splitter or Wollaston prism and balanced photodetectors. As the timing between pump and probe beam is changed by moving the delay stage, the terahertz field can be sampled by acquiring the polarization change of the probe beam.

In electro-optic detection, the detection bandwidth is limited by the absorption profile and thickness of the nonlinear crystal. The phonon resonances in nonlinear crystals may limit the bandwidth. Additionally, the group velocity mismatch between the optical probe and terahertz beams may decrease the electro-optic detection responsivity. The most common crystals used for terahertz detection at 800 nm optical wavelength are ZnTe and GaP. ZnTe has a very good velocity match at 1 THz, and GaP has one at 6 THz [30, 31]. The bandwidth of ZnTe is limited by a phonon resonance occurring at 5.3 THz. For this reason, ZnTe is usually used for detection in the 0.1-3 THz frequency range, and GaP is used for the 3-8 THz range. (111) GaAs crystal is used to detect in the range of 0.1-3 THz for systems with 1550 nm lasers [32]. At higher terahertz frequencies, velocity mismatch increases. Therefore, thinner crystals are used at the expense of losing responsivity at lower terahertz frequencies.

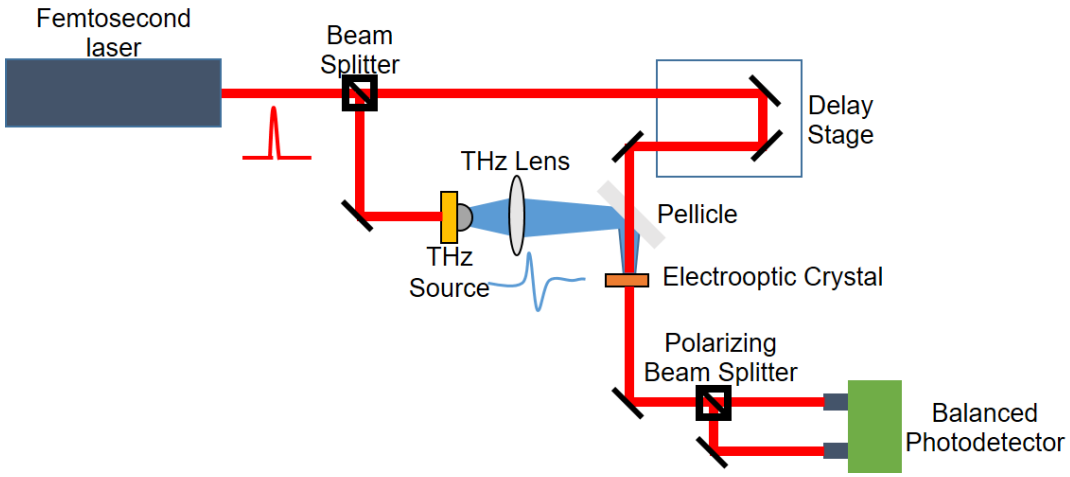

Figure 1.4. A time-domain terahertz spectroscopy setup with electro-optic detection.

Rather than bandwidth concerns, one problem with electro-optic detection is the necessity of using some extra optical components to sense the change in polarization of the probe beam. This can be an issue for the realization of compact time-domain terahertz systems.

1.4.2 Pulsed Terahertz Detection through Photoconductive Detectors

Detection through photoconductive devices is another technique for sub-picosecond pulse detection [34-36]. Compared to electro-optic detection, it offers a more compact solution by eliminating the need for extra optical components to sense the polarization change of the probe beam in the case of electro-optic detection. A conventional photoconductive detector, similar to a conventional photoconductive source, uses a short-carrier-lifetime semiconductor as an ultrafast photoconductor. A terahertz antenna is fabricated on the semiconductor. The active area of the detector is illuminated by the femtosecond optical beam, and electron-hole pairs are generated. No bias voltage is applied from the antenna electrodes. When a terahertz beam is incident on a photoconductive antenna, a terahertz electric field is induced across the photoconductor contact electrodes, drifting photo-generated carriers and inducing a photocurrent proportional to the incident terahertz field. As the delay stage moves to different positions, the timing of the pump and probe beam changes; thus, the strength of the induced photocurrent changes.

The amplitude of the terahertz field incident on the detector is weak in most applications. Therefore, the induced electric field within the device cannot be sufficiently high for photo-generated carriers to reach high drift velocities. This significantly limits the number of carriers reaching the contact electrodes before recombining inside the semiconductor. Therefore, the responsivity of conventional photoconductive detectors is very low. The detection bandwidth of photoconductive detectors is also bounded by factors such as antenna design, device parasitics, carrier lifetime and drift velocity. Thermal noise is the main noise source for photoconductive

detectors [37, 38]. Therefore, high-resistivity semiconductors should be used to achieve reasonable noise performance from the detectors.

1.5 Plasmonic Photoconductive Terahertz Sources and Detectors

Recently, it was shown that incorporating plasmonic contact electrodes in photoconductive devices significantly increases the quantum efficiency of the device [39-49]. Periodic plasmonic structures are usually used as contact electrodes to offer a much more efficient optical absorption profile. They are designed to provide the extra momentum necessary to excite surface plasmon waves when an optical beam is incident on them [24, 52]. When the optical transmission occurs through surface plasmon wave excitation, most of the carriers are generated very close to the contact electrodes. In this case, if the photoconductive device is a source and a bias voltage is applied through the contact electrodes, much more of the photo-generated carrier can reach the contact electrodes before recombining in the semiconductor. Therefore, a much stronger terahertz radiation with a much higher optical-to-terahertz conversion efficiency can be achieved compared to conventional photoconductive sources. Similarly, for detectors, the plasmonic enhancement results in inducing stronger photocurrents due to the large number of carriers that can be drifted to the contact electrodes. This increases the detector sensitivity and responsivity significantly. By using plasmonic gratings, the optical-to-terahertz conversion efficiency of photoconductive sources and the detection sensitivity of photoconductive detectors can be enhanced by 50 and 30 times, respectively [40]. A record-high optical-to-terahertz conversion efficiency of 7.5% is obtained by using three-dimensional plasmonic structures [41]. By using an array of 3×3 plasmonic photoconductive terahertz sources with logarithmic spiral antennas, a pulsed terahertz radiation power level of 1.9 mW is achieved at an optical pump power level of

320 mW [46]. However, the radiation bandwidth is limited by the antenna frequency response and RC parasitics.

In this study, plasmonic structures are also used to offer superior optical absorption. The plasmonic structures are designed to operate as broadband terahertz nanoantenna arrays. These plasmonic nanoantenna arrays are fabricated on a large area to either serve as terahertz source or terahertz detector. The details of plasmonic nanoantenna arrays are given in the next chapters.

1.6 Outline of the Dissertation

The next chapters of this dissertation are organized as follows:

Chapter 2 introduces plasmonic nanoantenna arrays operating as pulsed terahertz sources and explains the design, fabrication and characterization of these devices. A proof-of-concept source is described in Section 2.1. Impact of semiconductor substrate characteristics is experimentally analyzed and discussed in Section 2.2. An enhanced photoconductive source design based on plasmonic nanocavities is presented in Section 2.3. A telecommunication-compatible plasmonic nanoantenna array is described in Section 2.4. Sections of this chapter also appeared in IEEE Transactions on Terahertz Science and Technology [50], Optics Express [51], Applied Physics Letters [53].

Chapter 3 is focused on terahertz detection by plasmonic nanoantenna arrays. A theoretical and experimental analysis of this type of detector is provided in this section. This study also appeared in Scientific Reports [54].

Chapter 4 summarizes and concludes the dissertation.

Chapter 2: Terahertz Generation through Large-Area Plasmonic Nanoantenna Arrays

2.1. Overview

As discussed in Chapter 1, the main limitations of time-domain terahertz systems are the low optical-to-terahertz conversion efficiency and narrow bandwidth of photoconductive sources. To address the optical-to-terahertz conversion efficiency limitation of source, we present a novel design based on plasmonic nanoantenna arrays. By incorporating two-dimensional plasmonic nanoantenna arrays in large-area photoconductive sources, most of the photocarriers are generated in close proximity to the contact electrodes. Therefore, majority of the photocarriers are drifted to the contact electrodes within a sub-picosecond time-scale. Plasmonic structures are also designed to serve as broadband terahertz radiation elements. Therefore, a much stronger time-varying dipole moment is induced in response to an incident optical pump and, thus, greatly-enhanced optical-to-terahertz conversion efficiency is achieved compared to conventional large-area photoconductive sources.

2.2. Sources Fabricated on Semi-Insulating GaAs Substrate

2.2.1 Source Design

The first device prototype is fabricated on a semi-insulating (SI) GaAs substrate with a 1×1 mm^2 device active area. The schematic diagram of the presented large-area photoconductive source based on two-dimensional plasmonic nanoantenna arrays is illustrated in Fig. 2.1.

The device consists of a set of interdigitated bias lines. Arrays of plasmonic nanoantennas are connected to the anode bias lines within every other gap between the anode and cathode bias lines. The other gaps between the anode and cathode bias lines are shadowed by a second metal layer deposited on top of a Si_3N_4 antireflection coating to block light transmission into the GaAs substrate and induce uni-directional dipole moment in the substrate [25].

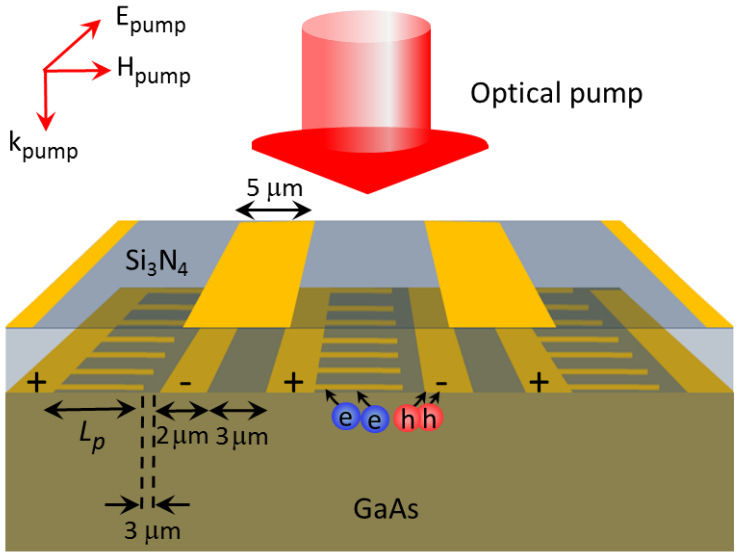

Figure 2.1. Schematic diagram and operation principles of the large-area plasmonic nanoantenna array fabricated on a SI-GaAs substrate.

The geometry of the plasmonic nanoantennas and thickness of the Si_3N_4 antireflection coating are chosen to transmit majority of the incident optical pump photons through the plasmonic nanoantennas into the SI-GaAs substrate [55]. A finite-element solver (COMSOL) is used to analyze the interaction of a TM-polarized optical beam with the designed plasmonic nanoantennas. The analysis shows that use of Au gratings with 200 nm pitch, 100 nm metal width, and 50 nm metal height and a 350 nm thick Si_3N_4 antireflection coating offers 79% optical transmission into the SI-GaAs substrate at 800 nm pump wavelength (Fig. 2.2).

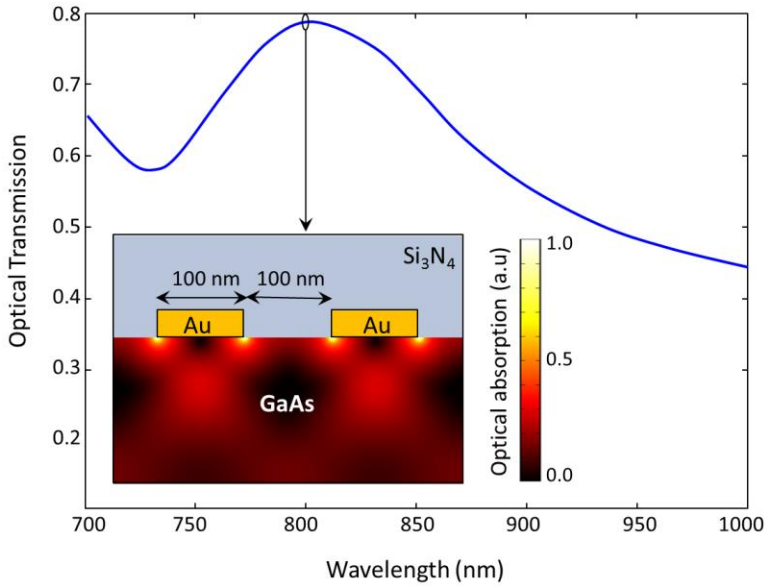

Figure 2.2. Power transmission of a TM-polarized optical beam into the SI-GaAs substrate as a function of optical wavelength. Inset shows color plot of optical absorption in the SI-GaAs substrate in response to a TM-polarized optical beam at 800 nm optical wavelength.

Since transmission of the incident optical pump into the SI-GaAs substrate is through excitation of surface plasmon waves and through 100 nm gaps between the plasmonic nanoantennas, a large portion of the photocarriers are generated very close to the contact electrodes. Therefore, a large portion of the photo-generated electrons drift to the anode contact electrodes within a sub-picosecond timescale and radiate through the effective Hertzian dipole formed by the plasmonic nanoantennas. To achieve a broad radiation bandwidth and prevent destructive photocurrent interference along the plasmonic nanoantennas, the length of the nanoantennas, Lp, is selected to be much shorter than the effective terahertz radiation wavelength. Compared to the conventional large-area photoconductive sources, photocurrent propagation velocity along plasmonic nanoantennas is not limited by the carrier scattering inside the semiconductor substrate lattice. Therefore, the Hertzian dipoles formed by the plasmonic nanoantennas offer significantly higher

radiation resistance and better impedance matching to free space compared with the radiating dipoles induced within the semiconductor substrate of conventional large area photoconductive sources [56].

Prototypes of large-area plasmonic nanoantenna arrays are fabricated and characterized to show the key role of plasmonic nanoantennas in offering high power terahertz radiation with significantly enhanced optical-to-terahertz conversion efficiencies. Nanoantenna lengths of 5 μm and 10 μm are chosen for the fabricated device prototypes to demonstrate the impact of the nanoantenna length on terahertz radiation bandwidth and efficiency. A gap of 3 μm is chosen between the tip of the anode contact electrode gratings and the cathode contact electrodes in all device prototypes. This will limit the operation of all device prototypes to the same breakdown bias voltage levels.

2.2.2 Source Fabrication

The fabrication process begins with patterning the plasmonic nanoantenna arrays using electron-beam lithography, followed by 5/45 nm Ti/Au deposition and liftoff. An optical lithography step with a bi-layer photoresist is used to pattern the bias lines, which is followed by 50/550 nm Ti/Au deposition and liftoff. The 350 nm Si3N4 anti-reflection coating is deposited using plasma-enhanced chemical vapor deposition (PECVD). The shadow metal is patterned next through optical lithography, followed by 10/90 nm Ti/Au deposition and liftoff. The contact vias are patterned using optical lithography and opened by etching the Si3N4 layer using reactive ion etching (RIE). Finally, the device prototypes are mounted on hyper-hemispherical silicon lenses and placed on an optical rotation mount to adjust the polarization of the optical pump with respect to the plasmonic nanoantennas. Figure 2.3 shows the scanning electron microscope

(SEM) images of a fabricated large-area plasmonic photoconductive nanoantenna array with 5 μm plasmonic nanoantenna (Figure 2.3a) and the plasmonic nanoantennas incorporated inside the device active area (Figure 2.3b).

(a) (b)

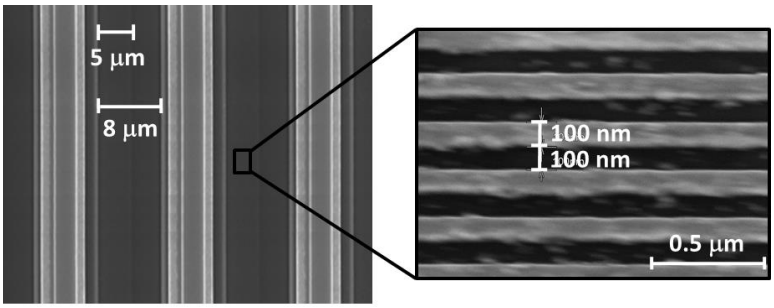

Fig. 2.3. The SEM image of a fabricated large-area plasmonic nanoantenna array with 5 μm long plasmonic nanoantennas, (b) SEM image of the plasmonic nanoantennas.

2.2.3 Source Characterization and Analysis

Terahertz radiation from the plasmonic nanoantenna array prototypes is characterized in response to an optical pump beam from a Ti:sapphire mode-locked laser at 800 nm wavelength, with a repetition rate of 76 MHz and a pulse width of 135 fs. Spot size of the optical pump beam is adjusted to illuminate the entire device active area and polarization of the optical pump beam is set to be normal to the plasmonic nanoantennas. A calibrated pyroelectric detector (Spectrum Detector, Inc. SPI-A-65 THz) is used to measure radiated power from the fabricated large-area plasmonic photoconductive source prototypes as a function of the bias voltage and optical pump power (P_{pump}). The pyroelectric detector is calibrated as explained in Ref. [57]. Figure 2.4 shows the impact of the nanoantenna length on performance of the large-area plasmonic photoconductive nanoantenna array prototypes.

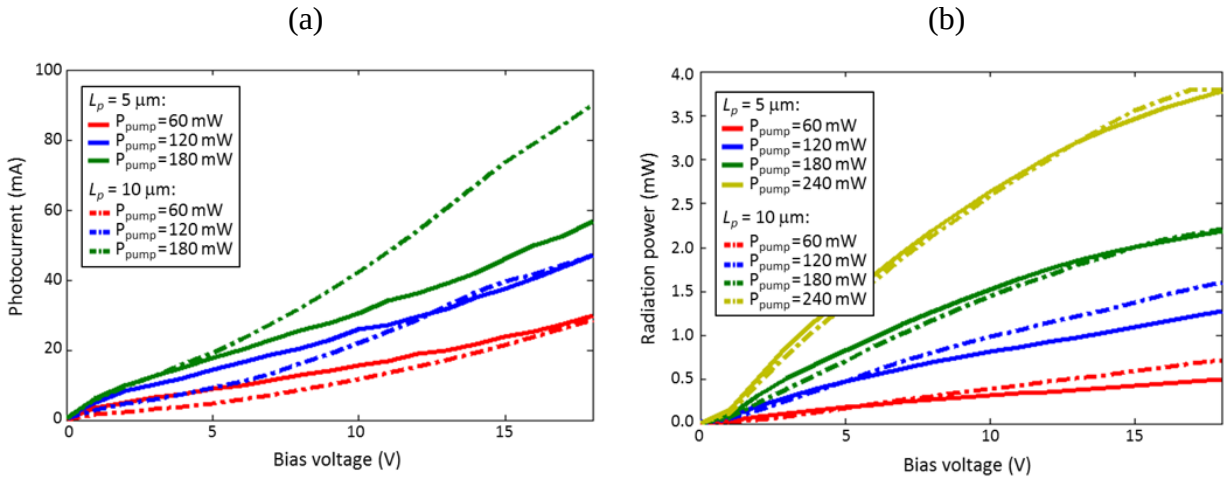

Figure 2.4. Photocurrent and radiated power for the large-area plasmonic nanoantenna arrays with 5 µm and 10 µm nanoantenna lengths fabricated on SI-GaAs substrate.

The photocurrent of the large area plasmonic nanoantenna arrays with 5 µm and 10 µm nanoantenna lengths fabricated on SI-GaAs substrate is shown in Figure 2.4a. At low optical pump powers and low bias voltage levels, the source prototypes with 5 µm nanoantenna length exhibit higher photocurrent levels compared to the source prototypes with 10 µm nanoantenna length. This is because of a more considerable bias electric field reduction along the 10 µm-long plasmonic nanoantennas in comparison with the 5 µm-long plasmonic gratings. Increasing the bias voltage level compensates the bias electric field reduction along the 10 µm-long plasmonic nanoantennas, leading to a reduction in the difference between the photocurrent of the sources with 5 µm and 10 µm nanoantenna lengths. While the bias electric field reduction along the 10 µm-long plasmonic nanoantennas becomes less effective as the bias voltage is increased further, the source prototypes with 10 µm nanoantenna length start exhibiting higher photocurrent levels compared to the source prototypes with 5 µm nanoantenna length. This trend, which is more obvious at higher optical pump power levels, is because the shadowed area in the sources with 10 µm nanoantenna length covers a smaller portion of the whole device area compared to the

sources with 5 µm nanoantenna length. Therefore, a larger number of photocarriers is generated within the active area of the sources with 10 µm nanoantenna length, leading to higher photocurrent levels under sufficient bias electric field levels.

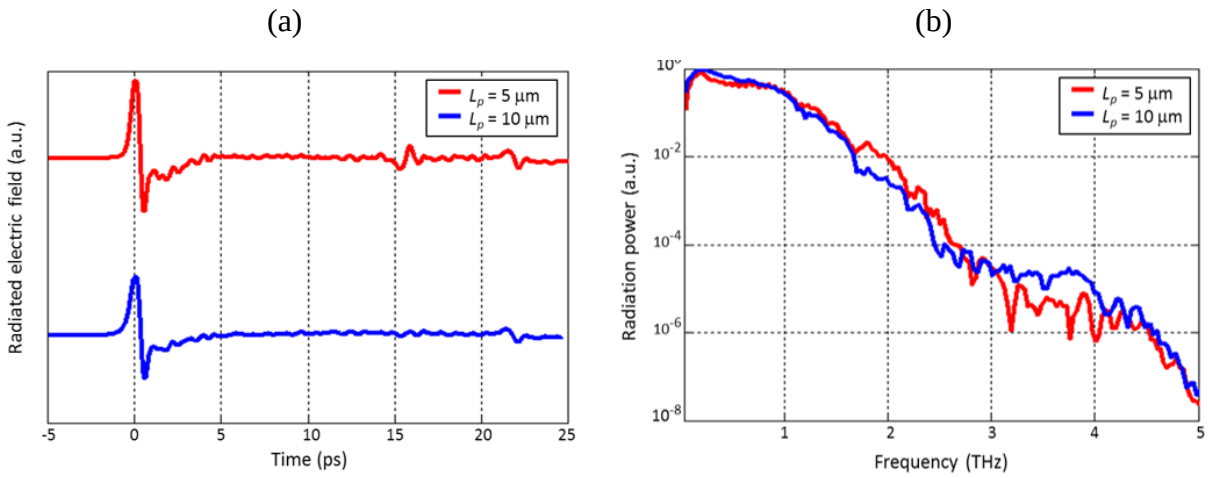

Figure 2.5. Radiated electric field in the time domain and radiated power in the frequency domain for the large area plasmonic photoconductive sources with 5 µm and 10 µm plasmonic grating lengths fabricated on SI-GaAs substrate.

The radiated power from the large-area photoconductive sources based on plasmonic nanoantenna arrays with 5 µm and 10 µm nanoantenna lengths fabricated on SI-GaAs substrate is shown in Figure 2.4b. At lower optical pump power levels and sufficient bias voltage levels, the sources with 10 µm nanoantenna length offer higher radiation power levels compared to the sources with 5 µm nanoantenna length. This is predicted since a larger number of photocarriers contribute to terahertz radiation when a smaller portion of the device active area is shadowed. At higher optical pump power levels, the sources with 10 µm nanoantenna length become less superior in offering higher radiation power levels. This is because the sources with 10 µm plasmonic nanoantenna length are more susceptible to suffer from the carrier screening effect

compared to the sources with 5 μm nanoantenna length. At an optical pump power of 240 mW and bias voltage of 18 V, both large-area sources with plasmonic nanoantenna arrays with 5 μm and 10 μm nanoantenna lengths offer 3.8 mW of radiation power.

The radiated electric field from the fabricated plasmonic nanoantenna arrays is measured in a time-domain terahertz spectroscopy setup with electro-optic detection in 1 mm ZnTe crystal. For this measurement, all the fabricated sources are characterized at 18 V bias voltage and 150 mW optical pump power. The radiated electric field in the time domain and radiated power in the frequency domain for the large-area plasmonic nanoantenna arrays with 5 μm and 10 μm nanoantenna lengths fabricated on SI-GaAs substrate are shown in Figure 2.5a and Figure 2.5b, respectively. At lower frequencies (f_{THz} < 1 THz), the sources with 10 μm nanoantenna length radiate higher terahertz power levels compared to the sources with 5 μm nanoantenna length. This is because a larger number of photocarriers are generated in close proximity to the contact electrodes for the sources with 10 μm nanoantenna length since a smaller portion of the device active area is shadowed. Therefore, a larger number of photocarriers are drifted to the contact electrodes within a fraction of the oscillation period of the terahertz radiation. Although a larger number of photocarriers are generated very close to the plasmonic structures for the sources with 10 μm nanoantenna length, the number of the photocarriers that are drifted to the contact electrodes within a fraction of the oscillation period of the terahertz radiation is not larger than that of the sources with 5 μm nanoantenna length at higher terahertz frequencies. This is because the sources with 10 μm nanoantenna length are more susceptible to suffer from the carrier screening effect and bias electric field reduction along the nanoantennas, which prevents ultrafast drift of the photocarriers to the contact electrodes. Therefore, the sources with 5 μm plasmonic nanoantenna length offer higher radiation power levels compared to the sources with 10 μm

plasmonic nanoantenna length at higher frequencies (fTHz > 1 THz). It should be noted that the higher terahertz radiation power levels offered by the sources with 10 μm nanoantenna length within 3-4 THz is due to the resonant behavior of the 10 μm-long nanoantennas, which behave like a quarter-wave monopole antenna within this frequency range.

2.3. Sources Fabricated on Short-Carrier-Lifetime Substrates

Although the two-dimensional plasmonic nanoantenna arrays fabricated on SI-GaAs offer very high optical-to-terahertz conversion efficiencies and terahertz radiation power levels over a broad frequency range, sources fabricated on short-carrier-lifetime substrates such as low-temperature-grown (LT) GaAs can offer more reliable performance. To grow short-carrier-lifetime semiconductors, deep level defects are added to the semiconductor lattice. The introduced defects lower the carrier lifetime and carrier drift velocity dramatically. While characteristics of the terahertz radiating elements, architecture of the photoconductors, and spectral properties of the optical pump beam have direct impact on performance of photoconductive terahertz sources [58], characteristics of the photo-absorbing semiconductor substrate are also crucial in determining specifications of the generated terahertz radiation. Desired photo-absorbing semiconductor substrates should have high carrier mobility and drift velocity levels to offer high optical-to-terahertz conversion efficiencies. They are also required to have high dark resistivity levels to allow device operation under high bias voltages to drift the photocarriers at saturation velocities while maintaining low dark current and thermal dissipation levels. Additionally, short carrier lifetimes are often required to eliminate negative impact of slow photocarriers that do not contribute to efficient terahertz generation but result in device heating and optical-to-terahertz conversion efficiency reduction due to the carrier screening effect and voltage drop across the device active area. Unfortunately, most techniques for

developing short carrier lifetime semiconductor substrates introduce high defect density levels inside the semiconductor lattice and, therefore, degrade the carrier mobility and drift velocity of the semiconductor substrate [59]. As a result, choosing optimum photo-absorbing semiconductor substrates for photoconductive terahertz sources requires an extensive analysis of the tradeoffs between substrate resistivity, carrier lifetime and drift velocity and their impact on terahertz radiation power, radiation bandwidth, thermal dissipation, and device reliability.

In this work, we study the impact of the photo-absorbing semiconductor substrate properties on the performance of large-area plasmonic nanoantenna arrays operating as pulsed terahertz sources at 800 nm wavelength. Large-area plasmonic nanoantenna arrays fabricated on SI-GaAs offer very high optical-to-terahertz conversion efficiencies and terahertz radiation power levels over a broad frequency range at 800 nm optical pump wavelengths because of the high carrier mobility and drift velocity of SI-GaAs. However, large-area plasmonic photoconductive nanoantenna arrays fabricated on short-carrier-lifetime substrates such as low-temperature-grown (LT) GaAs offer lower thermal dissipation and better reliability by recombining the slow photocarriers that do not contribute to efficient terahertz generation. Therefore, we study the use of various short-carrier-lifetime photo-absorbing semiconductor substrates in large area plasmonic photoconductive nanoantenna arrays to gain a deeper understanding of the impact of the substrate properties on terahertz radiation characteristics.

2.3.1 Material Growth

Materials based on LT-GaAs and superlattice structures of ErAs:GaAs, and LuAs:GaAs are used as the short carrier semiconductor substrates in our study. Recent studies have shown that epitaxially-embedded nanoparticles of rare-earth arsenide (RE-As) compounds, such as ErAs and

LuAs, can be used as recombination centers, decreasing the carrier lifetime dramatically [60-63]. Moreover, substrate resistivity, mobility, and carrier lifetime can be varied by controlling the RE-As deposition and the superlattice period thickness. ErAs:GaAs and LuAs:GaAs substrates with different RE-As depositions and superlattice periods/thicknesses are grown by solid-source molecular beam epitaxy (MBE) on semi- insulating (100) GaAs substrates.

Table 2.1. Carrier lifetime of the grown LT-GaAs, ErAs:GaAs, and LuAs:GaAs compounds.

Material	LT-GaAs	ErAs:GaAs (0.5ML/ 100A)×10 0	ErAs:GaAs (0.15ML/ 50A)×200	ErAs:GaAs (0.1ML/ 50A)×200	LuAs:GaAs (0.5ML/ 100A)×100	LuAs:GaAs (0.25ML/ 50A)×200	LuAs:GaAs (0.25ML/ 100A)×100
Carrier lifetime	0.3 ps	0.93 ps	0.67 ps	0.67 ps	0.8 ps	0.74 ps	0.65 ps

The ErAs:GaAs and LuAs:GaAs substrates are prepared by Laboratory for Advanced Semiconductor Epitaxy directed by Prof. Seth Bank at University of Texas at Austin. The structures are grown at 530 °C with an As_2/Ga beam equivalent pressure (BEP) ratio of 15 and 3 × 10^{-6} Torr BEP of As_2, which is held constant throughout the growth of the structures. RE-As nanoparticles are epitaxially incorporated in a superlattice structure with depositions of LuAs/ErAs nanoparticles repeated each period. The depositions are reported in terms of equivalent number of LuAs/ErAs monolayers (ML), as determined from reflection high-energy electron-diffraction (RHEED) intensity oscillations and high-resolution X-ray diffraction (HR-XRD) measurements of LuAs/ErAs films. After RE-As deposition, a 50 Å or 100 Å GaAs layer is grown and the structure is repeated 200 or 100 times, respectively. For comparison, a LT-GaAs substrate was grown at 250 °C with an As_2/Ga BEP ratio of 19, followed by an annealing process at 600 °C for 10 minutes. The carrier lifetime of the samples are obtained

through time-resolved differential optical pump- probe reflection measurements. A list of the materials used in our study together with their carrier lifetimes are shown in Table 2.1.

2.3.2 Source Design and Fabrication

Identical large-area plasmonic nanoantenna arrays are fabricated on the LT-GaAs, ErAs:GaAs, and LuAs:GaAs substrates. Figure 2.6a shows the schematic diagram of the fabricated large area plasmonic photoconductive sources. They are designed to have a 0.5 × 0.5 mm^2 active area and 5 µm-long plasmonic nanoantennas with 100 nm wide, 50 nm thick, 200 nm spacing Au electrodes and a 350 nm-thick Si_3N_4 antireflection coating layer.

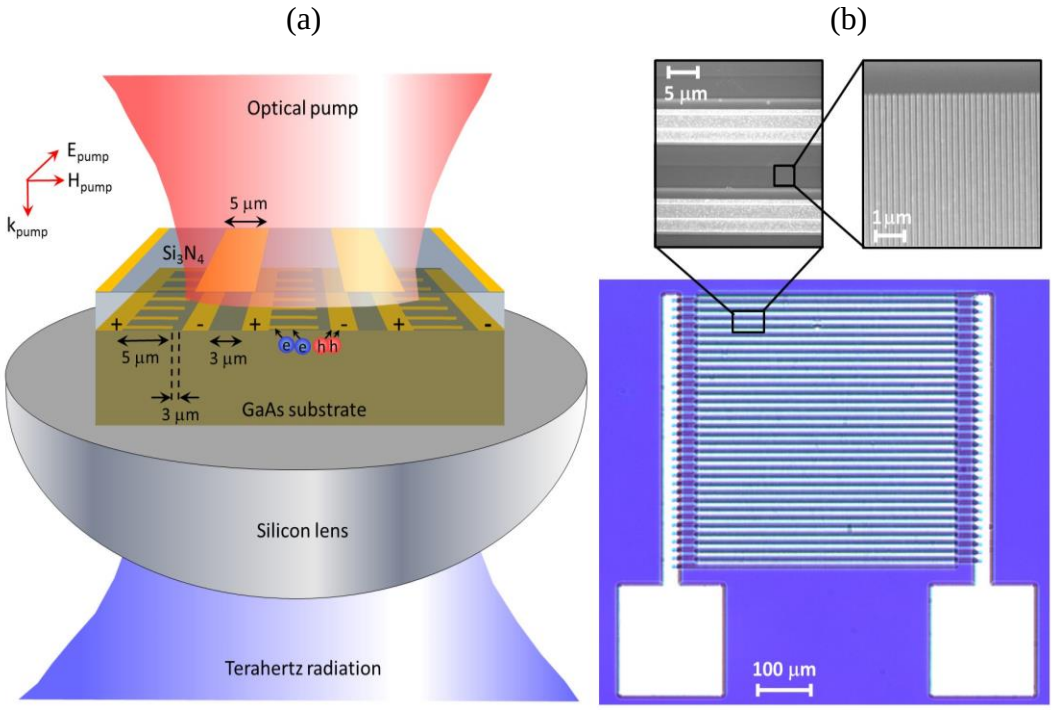

Figure 2.6. (a) Schematic diagram and operation concept of the fabricated large-area plasmonic photoconductive nanoantenna array sources. (b) Optical microscope and scanning electron microscope (SEM) images of a fabricated large-area plasmonic photoconductive nanoantenna array source prototype.

The same nanoantenna geometry that was used for the SI-GaAs sources is chosen to offer 79% power transmission into the GaAs substrate at 800 nm pump wavelength for a TM-polarized optical pump beam. The plasmonic nanoantennas are connected to anode bias lines of the photoconductive source within every other gap between the anode and cathode bias lines. The other gaps between the anode and cathode bias lines are shadowed by a second metal layer to block optical pump transmission into the GaAs substrate and prevent destructive interference with the generated terahertz radiation from the nanoantenna arrays.

The optical microscopy and scanning electron microscopy (SEM) images of a fabricated large-area plasmonic nanoantenna array prototype are shown in Figure 2.6b. The same fabrication process explained for the SI-GaAs sources is used for the nanoantenna array sources based on short-carrier-lifetime semiconductors. The device prototypes are mounted on hyper-hemispherical silicon lenses and placed on an optical rotation mount for optical pump polarization adjustments.

2.3.3 Source Characterization and Analysis

A mode-locked Ti:sapphire laser at 800 nm with 76 MHz repetition rate and 135 fs pulse width is used as a pump source to characterize the radiation properties of the fabricated nanoantenna arrays on different short-carrier lifetime substrates. The measured dark current and photocurrent of the fabricated large-area plasmonic nanoantenna prototypes are shown in Figure 2.7. While the photocurrent levels are directly proportional to the carrier drift velocity and carrier lifetime of the substrates, the dark current levels are directly affected by the resistivity of the substrates, which is a function of the carrier concentration and carrier drift velocity.

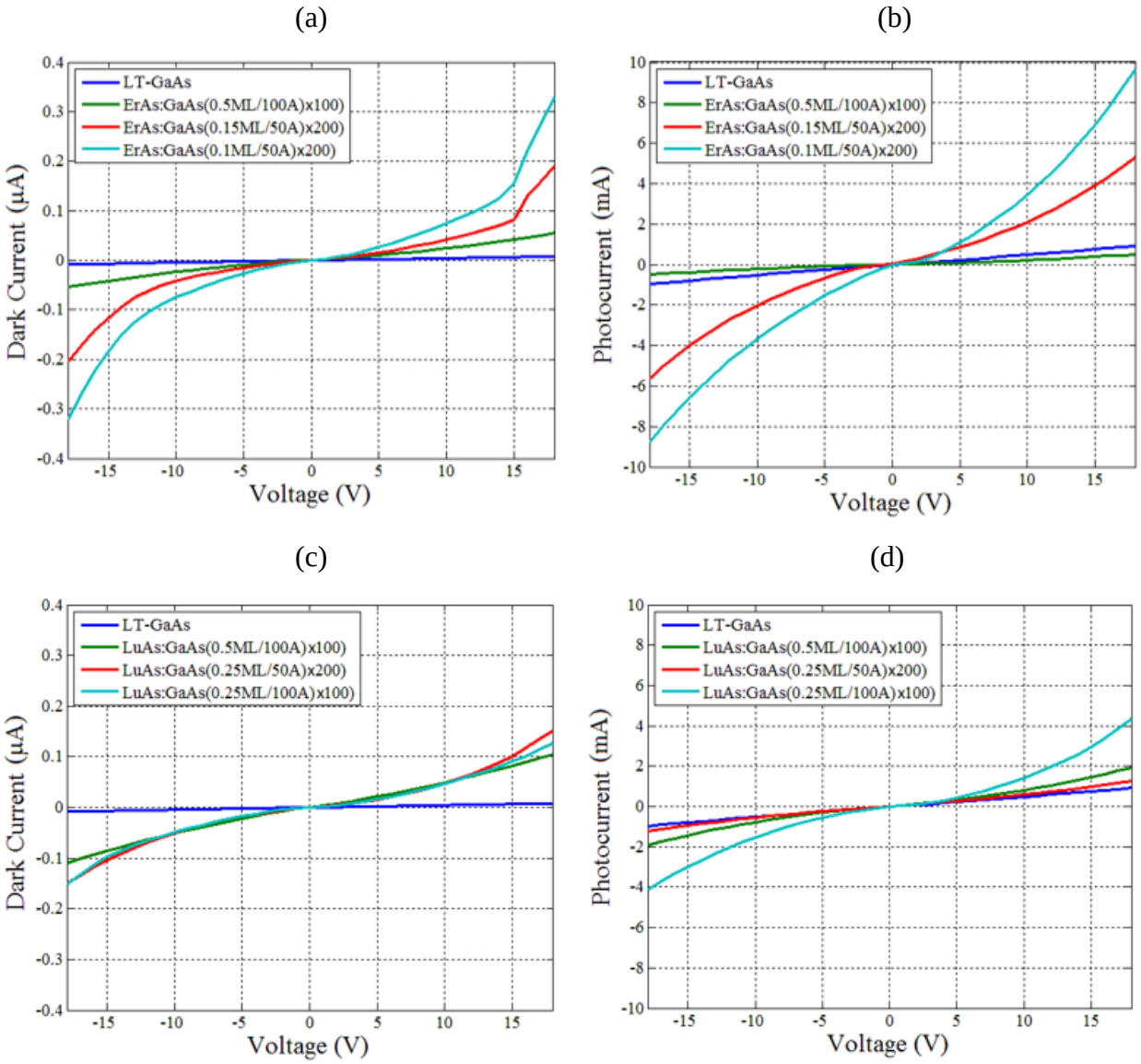

Figure 2.7. Measured dark current and photocurrent levels of the large-area plasmonic photoconductive nanoantenna arrays fabricated on the LT-GaAs and ErAs:GaAs substrates are shown in (a) and (b), respectively. Measured dark current and photocurrent levels of large-area plasmonic photoconductive nanoantenna arrays fabricated on the LT-GaAs and LuAs:GaAs substrates are shown in (c) and (d), respectively. Photocurrent levels are measured at 800 mW optical pump power.

A comparison between the dark current and photocurrent of the nanoantenna arrays fabricated on the LT-GaAs and ErAs:GaAs substrates is shown in Figures 2.7a and 2.7b, respectively. The results indicate a tradeoff between the substrate resistivity and carrier drift velocity for the ErAs:GaAs substrates with different ErAs depositions per superlattice period. The ErAs:GaAs samples with higher ErAs depositions exhibit higher substrate resistivities but offer lower carrier drift velocities, leading to lower induced photocurrent levels. This degrades photoconductive gain and optical-to-terahertz conversion efficiency of the large area plasmonic photoconductive sources fabricated on the ErAs:GaAs substrates with higher ErAs depositions. On the other hand, the low resistivity nature of the ErAs:GaAs substrates with lower ErAs depositions degrades device reliability and lifetime due to thermal breakdown caused by large dark current levels. Compared with the ErAs:GaAs substrates, the LT-GaAs substrate offers the highest substrate resistivity. Although the induced dark currents in the LT-GaAs sample are much smaller than the induced dark currents in the ErAs:GaAs samples, the induced photocurrent levels in the LT- GaAs sample are in the same order as those of the ErAs:GaAs (0.5ML/100Å) × 100 sample. Considering the carrier lifetime values of the LT-GaAs and ErAs:GaAs substrates, the measured photocurrent levels shown in Fig. 2(b) indicate that the carrier drift velocities in the LT-GaAs substrate are smaller but comparable with the ErAs:GaAs (0.15ML/50Å) × 200 and ErAs:GaAs (0.1ML/50Å) × 200 substrates but larger than the ErAs:GaAs (0.5ML/100Å) × 100 substrate.

A comparison between the dark current and photocurrent of the nanoantenna arrays fabricated on the LT-GaAs and LuAs:GaAs substrates is shown in Figures 2.7c and 2.7d, respectively. The results indicate similar substrate resistivity levels for the LuAs:GaAs substrates with different LuAs depositions per superlattice period, which are much smaller than the resistivity level of the

LT-GaAs substrate. Considering the carrier lifetime values of the LuAs:GaAs substrates, the measured photocurrent levels shown in Fig. 2(d) indicate that the carrier drift velocities in the LuAs:GaAs (0.25ML/100Å) × 100 substrate are much larger than other LuAs:GaAs substrates. This makes the LuAs:GaAs (0.25ML/100Å) × 100 substrate a more promising material for large area plasmonic nanoantenna array sources, by offering higher photoconductive gain and optical-to-terahertz conversion efficiency levels, accordingly. Considering the carrier lifetime values in the LT-GaAs and LuAs:GaAs substrates, the measured photocurrent levels shown in Fig. 2(d) indicate that the carrier drift velocities in the LT-GaAs substrate are comparable with the LuAs:GaAs (0.5ML/100Å) × 100 and LuAs:GaAs (0.25ML/50Å) × 200 substrates and smaller than the LuAs:GaAs (0.25ML/100Å) × 100 substrate. However, the high resistivity of the LT-GaAs substrate offers better operational reliability due to lower dark currents.

The radiated terahertz power from the large-area plasmonic nanoantenna array prototypes is measured by using a calibrated pyroelectric detector (Spectrum Detector, Inc. SPIA-65 THz) [57]. A comparison between the radiated terahertz power levels from the nanoantenna arrays fabricated on the LT-GaAs and ErAs:GaAs substrates at 800 mW optical pump power is shown in Figure 2.8a. As predicted from the photocurrent measurements, the source fabricated on the ErAs:GaAs (0.5ML/100A) × 100 substrate generates the lowest terahertz radiation power levels due to its low carrier drift velocities. In addition, the source fabricated on the ErAs:GaAs (0.1ML/50A) × 200 substrate generates the highest terahertz radiation power levels due to its high carrier drift velocities.

A comparison between the radiated terahertz power levels from the nanoantenna arrays fabricated on the LT-GaAs and LuAs:GaAs substrates at 800 mW optical pump power is

shown in Figure 2.8b. As expected, similar terahertz power levels are generated from the large-area plasmonic nanoantenna arrays fabricated on the LT-GaAs, LuAs:GaAs (0.5ML/100A) × 100 and LuAs:GaAs (0.25ML/50A) × 200 substrates due to their comparable carrier drift velocities. The source prototype fabricated on the LuAs:GaAs (0.25ML/100A) × 100 substrate generates the lowest terahertz radiation power levels at low bias voltages despite its high carrier drift velocities. This is due to the carrier screening effect, which impacts the LuAs:GaAs (0.25ML/100A) × 100 sample more severely due to its higher carrier drift velocity. However, this carrier screening effect is mitigated at higher bias voltages and is demonstrated by the higher terahertz output powers for voltages above 18 V.

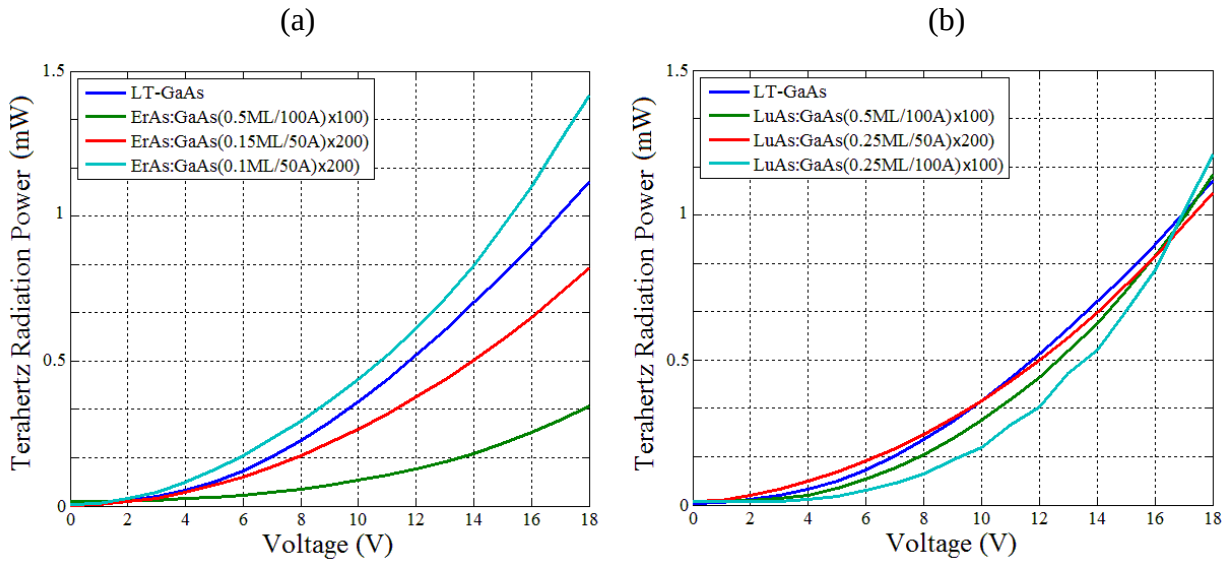

Figure 2.8. (a) Measured terahertz power levels at 800 mW optical pump power for the large-area plasmonic photoconductive nanoantenna arrays fabricated on the LT-GaAs and ErAs:GaAs substrates. (b) Measured terahertz power levels at 800 mW optical pump power for the large-area plasmonic photoconductive nanoantenna arrays fabricated on the LT-GaAs and LuAs:GaAs substrates.

As expected, the reliability and lifetime of the large area photoconductive sources with two-dimensional plasmonic nanoantenna arrays are directly impacted by their substrate resistivity and photocurrent levels. Thermal breakdown is observed for the large-area plasmonic nanoantenna array prototypes fabricated on the ErAs:GaAs (0.1ML/50A)×200, ErAs:GaAs (0.15ML/50A)×200, and LuAs:GaAs (0.25ML/100A)×100 substrates at 0.9 W, 1 W, and 1.1 W optical pump power levels, respectively. No thermal breakdown is observed for the rest of the large area plasmonic nanoantenna array prototypes up to 1.2 W optical pump power level.

A time-domain terahertz spectroscopy setup with electro-optic detection in a 1 mm ZnTe crystal is used to characterize radiated electric field from the large-area plasmonic photoconductive nanoantenna array prototypes [34]. In order to prevent thermal breakdown, the source prototypes fabricated on the ErAs:GaAs (0.1ML/50A)×200, ErAs:GaAs (0.15ML/50A)×200, and LuAs:GaAs (0.25ML/100A)×100 substrates are pumped at 800 mW optical pump power and the rest of the source prototypes are pumped at 1.15 W optical pump power. A bias voltage of 18 V is used for all the measurements. A comparison between the time-domain radiated fields from the source prototypes fabricated on the LT-GaAs substrate and the time-domain radiated fields from the source prototypes fabricated on the ErAs:GaAs and LuAs:GaAs substrates is shown in Figure 2.9a and Figure 2.9b, respectively. As expected, higher terahertz field levels are radiated from the source prototypes fabricated on the substrates with higher carrier drift velocity levels at the same optical pump powers. As an example, at 1.15 W optical pump power, higher terahertz field levels are radiated from the source prototypes fabricated on the LT-GaAs substrate compared to the source prototypes fabricated on the ErAs:GaAs (0.5ML/100A)×100 substrate. Similarly, at 800 mW optical pump power, higher terahertz field levels are radiated from the source prototypes fabricated on the ErAs:GaAs (0.1ML/50A)×200 substrate compared to the

source prototypes fabricated on the ErAs:GaAs (0.15ML/50A)×200 substrate. Additionally, at 1.15 W optical pump power, similar terahertz field levels are radiated by the source prototypes fabricated on the LT-GaAs, LuAs:GaAs (0.5ML/100A)×100, and LuAs:GaAs (0.25ML/50A)×200 substrates.

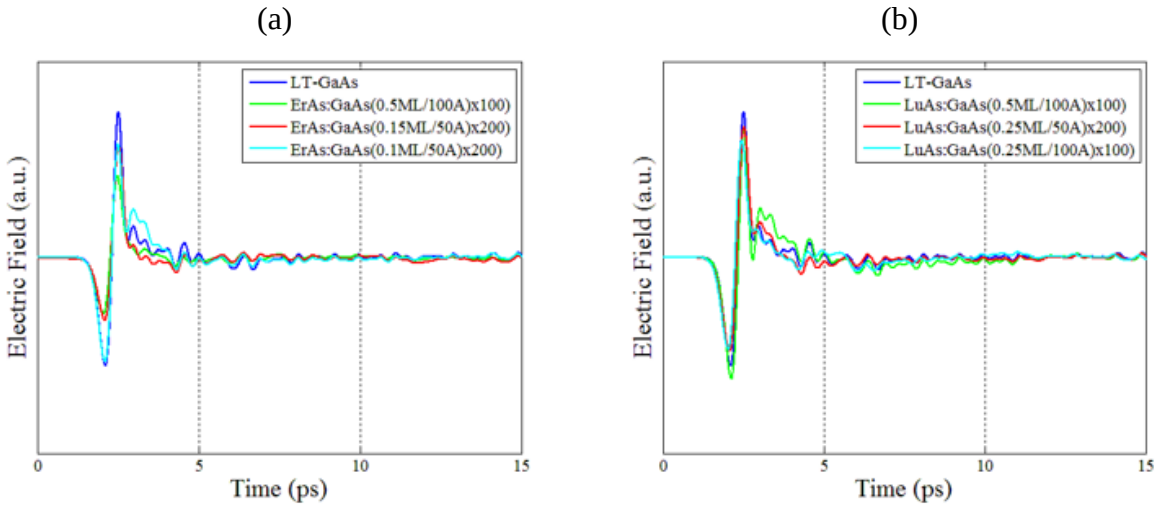

Figure 2.9. (a) Radiated electric field in the time domain from the large-area plasmonic nanoantenna array sources fabricated on the LT-GaAs and ErAs:GaAs substrates. (b) Radiated electric field in the time domain from the large-area plasmonic nanoantenna array sources fabricated on the LT-GaAs and LuAs:GaAs substrates.

The direct impact of the carrier drift velocity on the generated terahertz radiation is also confirmed by comparing the radiation spectra from the source prototypes fabricated on the LT-GaAs substrate and the radiation spectra from the source prototypes fabricated on the ErAs:GaAs and LuAs:GaAs substrates, as shown in Fig. 2.10a and Fig. 2.10b, respectively. Since the major portion of the generated terahertz radiation from the large-area plasmonic nanoantenna arrays is due to the ultrafast photocurrent fed to the nanoantenna arrays [50], similar radiation spectral shapes are obtained from the source prototypes fabricated on the LT-GaAs, ErAs:GaAs, and

LuAs:GaAs substrates. In the meantime, since the photocurrent levels fed to the nanoantenna arrays are directly proportional to the carrier drift velocity levels, higher terahertz radiation power levels are offered by the sources fabricated on the substrates with higher carrier drift velocity levels at the same optical pump powers.

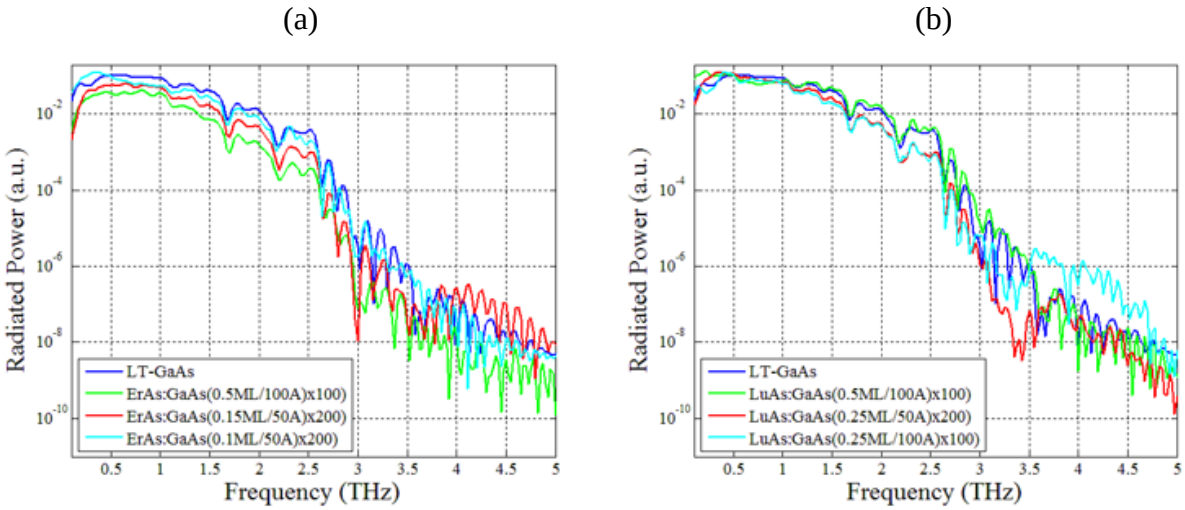

Figure 2.10. (a) Radiated spectra from the large-area plasmonic nanoantenna array sources fabricated on the LT-GaAs and ErAs:GaAs substrates. (b) Radiated spectra from the large-area plasmonic nanoantenna array sources fabricated on the LT-GaAs and LuAs:GaAs substrates.

2.4. Plasmonic Nanocavity Sources

Although source prototypes fabricated on short-carrier-lifetime semiconductors offer better reliability and thermal performance, the radiated power levels and optical-to-terahertz conversion efficiencies are much lower than source prototypes fabricated on SI-GaAs. To achieve high optical-to-terahertz conversion efficiency and low thermal dissipation, a novel photoconductive terahertz source is presented. This source overcomes the slow carrier problem by means of a nanocavity that induces the three-dimensional confinement of the optical pump light around the terahertz radiating elements. The source is fabricated on a thin, low-defect, high-mobility

semiconductor layer, which is grown on a substrate with a distributed Bragg reflector (DBR) structure. It consists of a two-dimensional array of plasmonic nanoantennas fabricated on the active high-mobility semiconductor layer. The plasmonic nanoantennas are specifically designed to excite surface plasmon waves at the optical pump wavelengths, while serving as radiating elements at terahertz frequencies [50]. The plasmonic structures and DBR layer are designed to form a nanocavity to tightly confine the optical pump beam inside the active high-mobility semiconductor layer. Therefore, when an optical beam pumps the device, almost all carriers are generated in very close proximity to the nanoantennas. If a bias voltage is simultaneously applied, almost all of the photo-generated carriers can reach the nanoantennas and contribute to generating an ultrafast current. As this strong ultrafast current drives the terahertz nanoantennas, a much more efficient optical-to-terahertz conversion occurs compared to the source prototypes discussed in the previous sections, and a powerful terahertz pulse can be generated. In addition, by mitigating the effect of slow carriers, robust operation of this source can be achieved.

2.4.1 Source Design and Fabrication

A schematic diagram of the presented terahertz source is illustrated in Figure 2.11. The source is mounted on a hemispherical silicon lens with a diameter of 12 mm. The DBR structure is grown on a semi-insulating GaAs substrate. It consists of 25 alternating pairs of 60 nm thick AlAs and 55 nm thick $Al_{0.33}Ga_{0.67}As$ layers. The plasmonic nanoantenna array is fabricated over an area of 1×1 mm^2 on the undoped top GaAs layer of 190 nm in thickness. A 262 nm thick $Al_{0.31}Ga_{0.69}As$ layer is used as a buffer layer between the top active GaAs layer and the DBR. Each plasmonic nanoantenna array is connected to the anode bias lines to take advantage of high-speed electrons rather than holes. A silicon nitride anti-reflection coating is deposited on the nanoantennas to further enhance the transmission of optical pump beam to the top active GaAs layer.

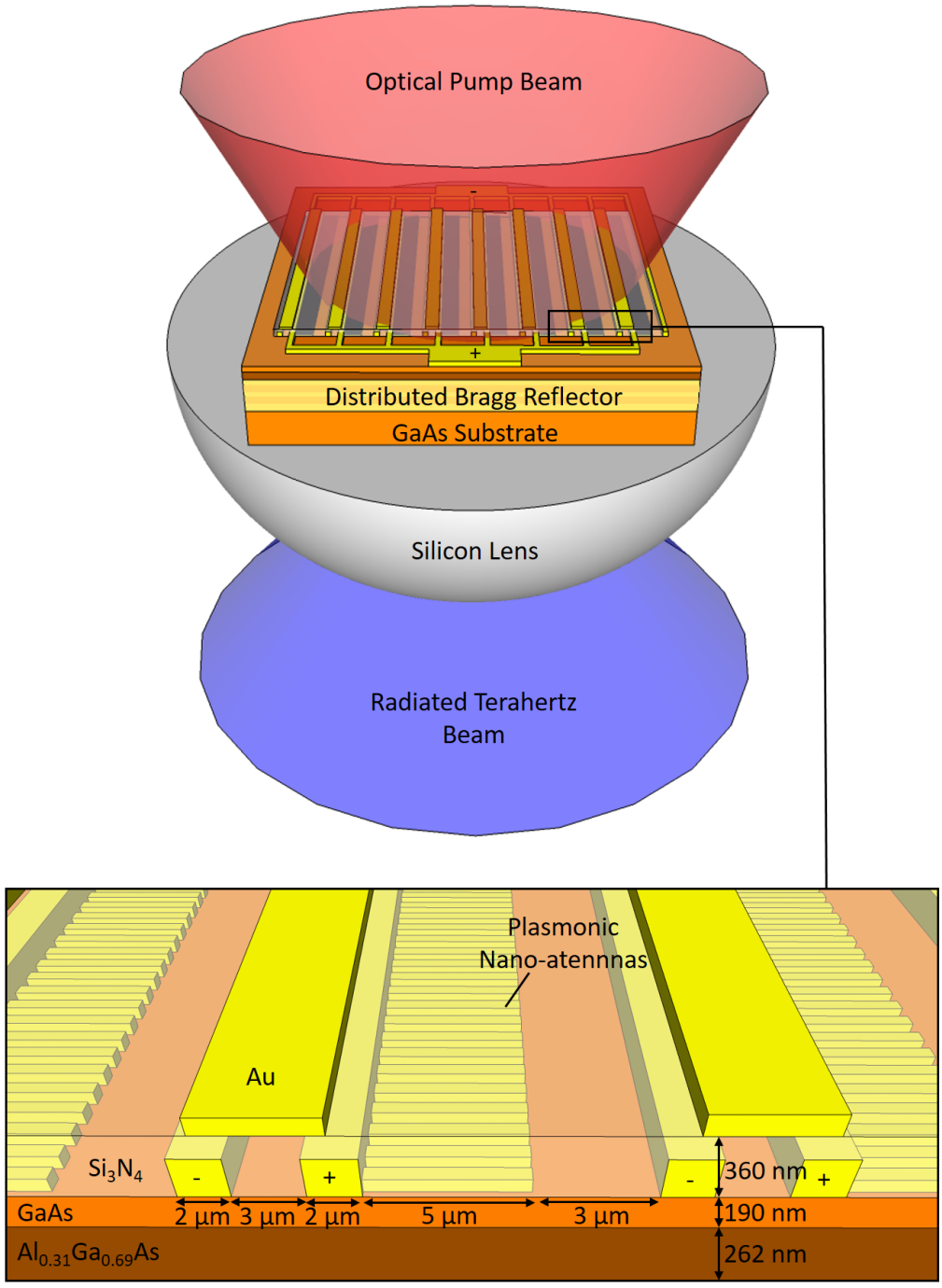

Figure 2.11. Schematic diagram and operation principle of the presented photoconductive source based on a nanocavity formed by a plasmonic nanoantenna array and DBR structure.

Every other gap between the anode and cathode bias lines is shadowed by an additional layer of metal deposited on top of the anti-reflection coating. This prevents generation of any ultrafast current in the opposite direction to the current driving the nanoantennas.

The plasmonic nanoantennas and DBR structure are designed to confine the incident optical pump beam in the top active GaAs layer. The interaction between plasmonic nanoantennas integrated with this particular semiconductor structure and a TM-polarized optical pump beam is analyzed using an electromagnetic simulation software based on the finite-difference time-domain method (Lumerical). The analysis is performed for a grating-shaped Au plasmonic nanoantenna array with a periodicity of 200 nm, a metal width of 100 nm and a metal height of 80 nm as well as a 360 nm-thick Si_3N_4 anti-reflective coating. The grating geometry is specifically selected to achieve zero optical reflection at a pump wavelength of 775 nm (Figure 2.12a). This means that all incident photons at this wavelength are trapped inside the semiconductor. Of the 775 nm incident photons, 78% are absorbed by the top active GaAs layer, whereas the rest are dissipated as a result of plasmonic losses. A two-dimensional color plot of the optical absorption inside the substrate at this wavelength is shown in Figure 2.12b. The enhancement in the optical absorption immediately below each nanoantenna proves that optical transmission is accompanied by the excitation of surface plasmon waves at 775 nm. The formation of a standing wave in the substrate indicates the resonant nature of the designed nanocavity. Considering that the entirety of the optical absorption occurs only in the top 190 nm thick GaAs volume immediately below the nanoantennas, most carriers will contribute to the radiation at terahertz frequencies, and there will be almost no carriers adding low-frequency components to the radiation in such a device structure. To achieve broadband radiation from the

terahertz nanoantennas, the length of the nanoantennas is chosen to be much smaller than the wavelengths of the terahertz spectral region (5 μm).

(a)

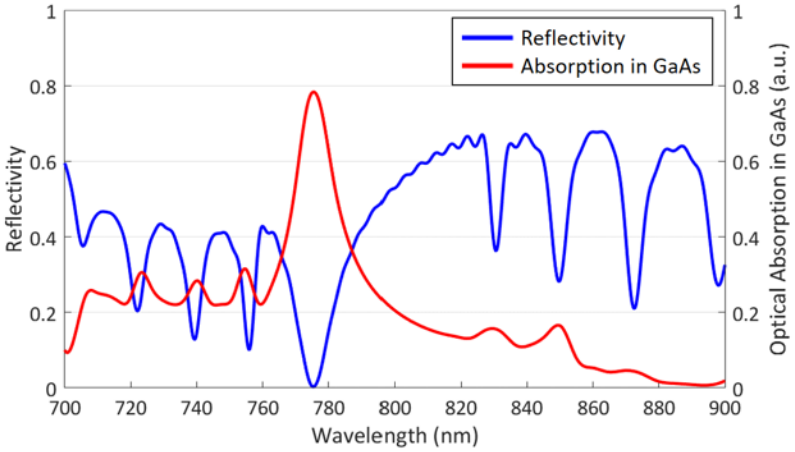

(b)

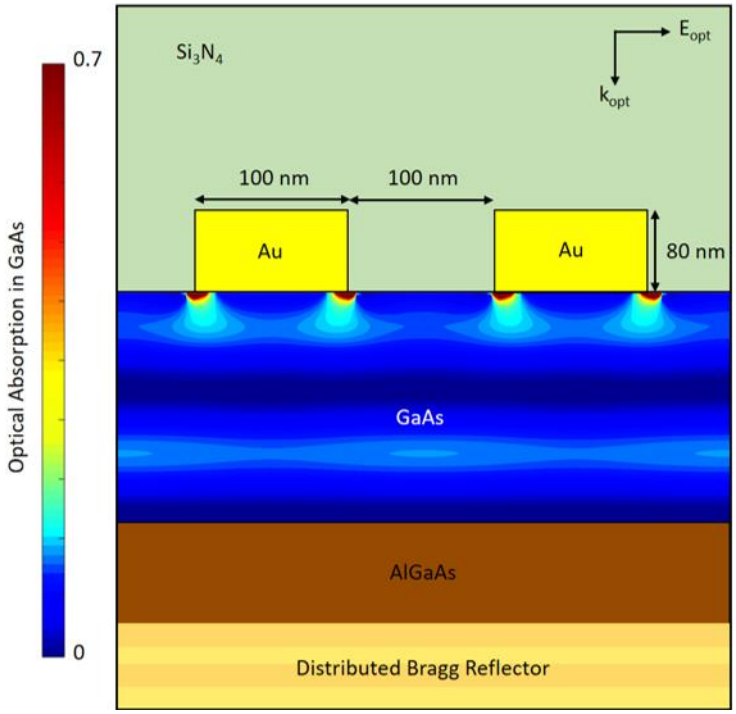

Figure 2.12. (a) The reflectivity of the designed plasmonic nanoantennas and the optical absorption in the top GaAs region as a function of the wavelength. (b) Two-dimensional color plot of the optical absorption in the top GaAs region at a wavelength of 775 nm.

The DBR structure, the AlGaAs buffer layer and the top GaAs layer are grown on a GaAs substrate via molecular beam epitaxy and used for fabricating a terahertz source prototype. The fabrication process begins with electron beam lithography for patterning the plasmonic terahertz nanoantennas. A metal evaporator is used to deposit a 2 nm-thick Ti adhesive layer and a 78 nm-thick Au layer. This is followed by a lift-off process for the formation of the nanoantennas. Subsequently, optical lithography is used to pattern the anode and cathode bias lines. Then, 50 nm/550 nm Ti/Au bias lines are formed by depositing the metals via evaporation, followed by a lift-off process. A 360 nm-thick Si3N4 anti-reflection layer is coated onto the device via plasma-enhanced chemical vapor deposition. Then, 10 nm/90 nm Ti/Au shadow metals are patterned via optical lithography, deposited via evaporation and formed using a lift-off process. The contact vias are opened by etching the Si3N4 layer via reactive-ion etching. Figure 2.13 shows an optical microscopy image of the entire terahertz source and scanning electron microscopy images of the plasmonic nanoantennas as well as the bias lines and shadow metals.

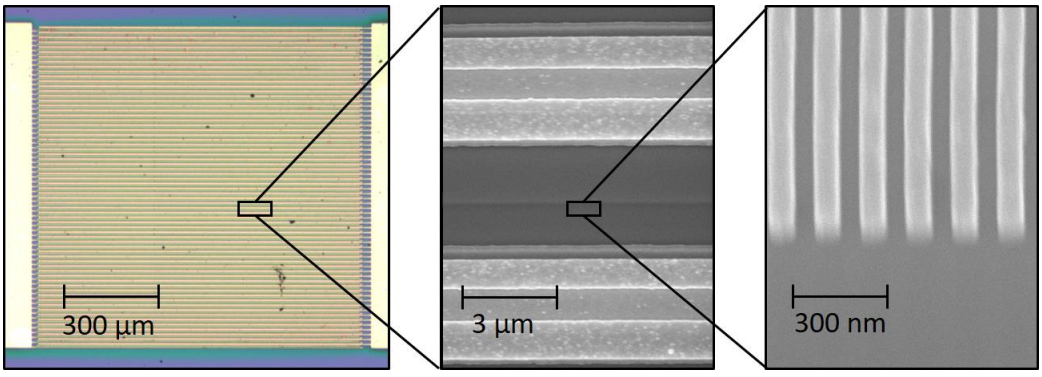

Figure 2.13. Optical microscopy image of the terahertz source prototype and scanning electron microscopy images of the bias lines, shadow metals and plasmonic nanoantennas.

2.4.2 Source Characterization

To experimentally prove that the nanocavity operates as designed, the optical reflection from the plasmonic nanoantennas is measured. To measure the optical reflectivity, another sample consisting only of plasmonic nanoantennas with a length of 0.1 mm and a Si_3N_4 anti-reflection coating, covering an area of 0.1×0.1 mm^2, is fabricated on the same substrate. A Ti:sapphire laser is used in continuous-wave (CW) operation mode. The polarization of the optical beam is set normal to the nanoantennas, and the spot size of the beam is adjusted to focus on the area covered by the plasmonic nanoantennas. The reflectivity is measured under an optical pump power of 10 mW, and the wavelength of the incident pump beam is swept from 740 nm to 820 nm. The measured and estimated optical reflectivity from the simulation results are compared in Figure 2.14a. The minimum measured reflectivity (~10%) is observed at 770 nm, corresponding to a slight blue shift compared with the estimated reflectivity. The increase in the minimum reflectivity and the shift in wavelength can be attributed to fabrication imperfections and small deviations in the thickness and composition of the grown semiconductor substrate layers from the intended design.

Subsequently, the photocurrent in the fabricated terahertz source prototype is measured using a CW optical beam with the same polarization. An optical pump power of 10 mW is used to illuminate the device. A bias voltage of 5 V is applied via the bias lines. As expected, a shift in wavelength similar to that observed for the reflectivity is also seen between the maximum measured photocurrent and the maximum optical absorption in the top GaAs layer as estimated from the simulations, for the same reasons described above (Figure 2.14b).

To demonstrate the superior performance of the presented terahertz source, a LT-GaAs plasmonic nanoantenna array with the design described in Section 2.3 is also fabricated and its performance is compared with the presented terahertz source prototype. To ensure a fair comparison, both sources are fabricated with the same active area, the same ratio between the active and shadowed areas, and the same nanoantenna length.

(a)

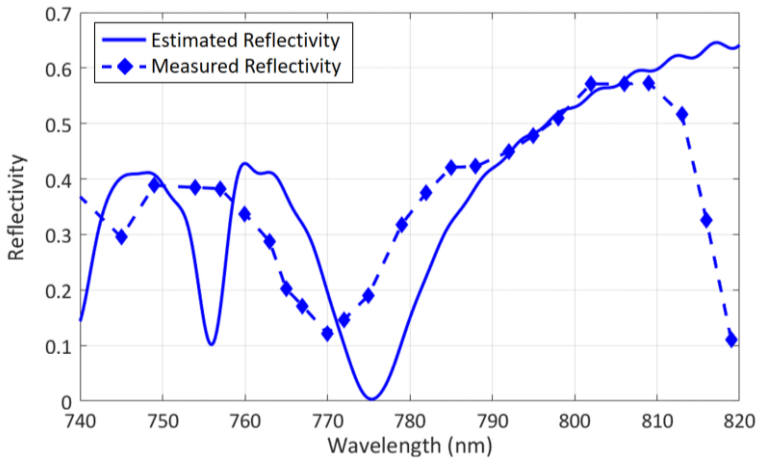

(b)

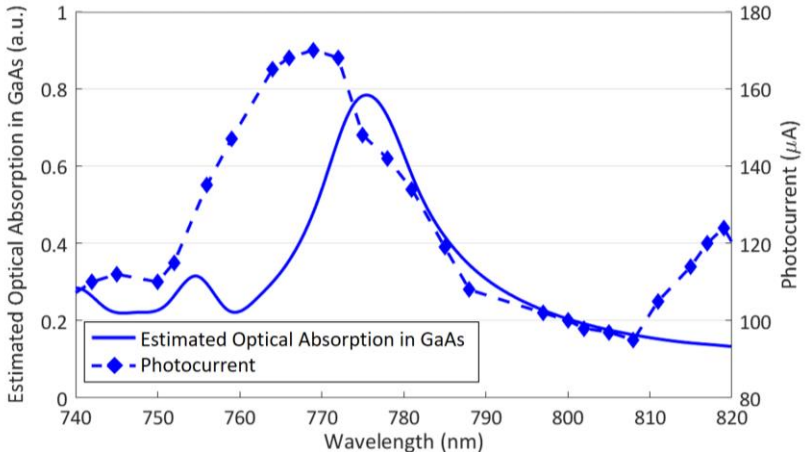

Figure 2.14. (a) The estimated and measured optical reflectivities of the plasmonic nanoantennas as a function of the wavelength. (b) The estimated optical absorption in the top GaAs layer and the measured photocurrent in the terahertz source prototype.

To measure the terahertz radiation characteristics, the operation mode of the Ti:sapphire laser is changed to mode-locked and the fabricated terahertz sources are pumped by 135 fs-wide optical pulses with a 76 MHz repetition rate, at a center wavelength of 770 nm.

(a)

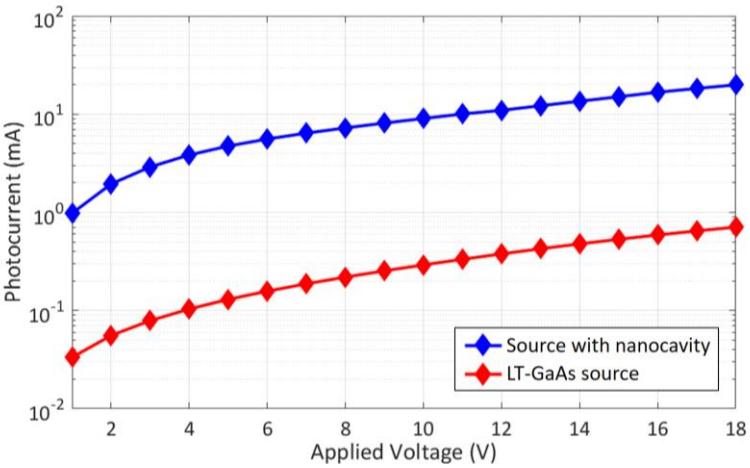

(b)

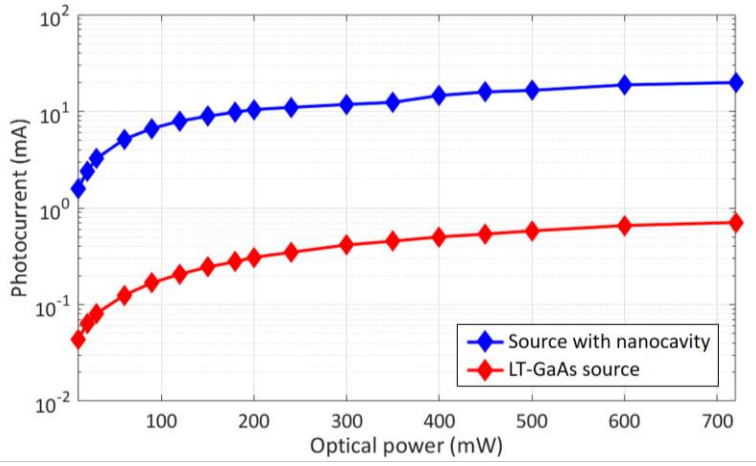

Figure 2.15. (a) Photocurrents in the nanocavity-based terahertz source and the terahertz source fabricated on the LT-GaAs substrate as a function of the bias voltage under an optical pump power of 720 mW. (b) Photocurrents in the nanocavity-based terahertz source and the terahertz source fabricated on the LT-GaAs substrate as a function of the optical pump power under a bias voltage of 18 V.

First, the photocurrents in the terahertz sources are measured. Figure 2.15a shows the measured photocurrent as a function of the bias voltage under an optical pump power of 720 mW. The nanocavity-based source exhibits a photocurrent that is 28 times stronger than that of the source fabricated on the LT-GaAs substrate. This stronger photocurrent can be attributed to the tighter light confinement near the plasmonic nanoantenna arrays and the higher carrier drift velocity offered by the low-defect semiconductor used in the nanocavity-based source. Figure 2.15b shows the photocurrent as a function of the optical pump power under a bias voltage of 18 V. At an optical pump power of 10 mW, the photocurrent is enhanced by a factor of 36 for the nanocavity-based source compared with the source fabricated on the LT-GaAs substrate. The enhancement factor slightly decreases to 28 under an optical pump power of 720 mW. This slight reduction can be attributed to the stronger carrier screening and scattering due to the larger number of photo-generated carriers in the active region of the nanocavity-based source compared with the carriers in the LT-GaAs-based source.

The radiated terahertz power is measured using pyroelectric detectors. Power levels higher than 20 μW are measured using a pyroelectric detector from Applied Physics and Electronics, Inc. (A.P.E. THz-30) calibrated at the Physikalisch-Technische Bundesanstalt (the German National Metrology Institute) and power levels lower than 20 μW are measured using another pyroelectric detector from Spectrum Detector, Inc. (SPIA-65 THz) calibrated using the A.P.E. THz-30 pyroelectric detector at a terahertz radiation power level of 20 μW. Figure 2.16a shows the radiated terahertz power levels of the two sources as a function of the bias voltage under an optical pump power of 720 mW. The measured terahertz radiation from the nanocavity-based source is 21 times stronger than that from the source fabricated on the LT-GaAs substrate.

(a)

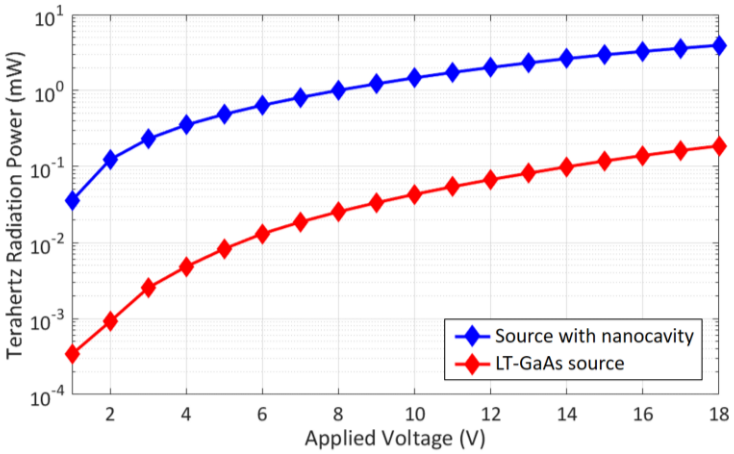

(b)

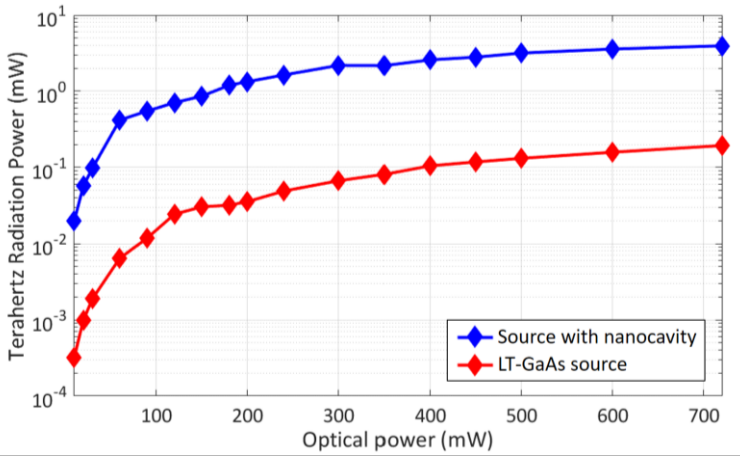

Figure 2.16. (a) Radiated terahertz power levels of the nanocavity-based terahertz source and the terahertz source fabricated on the LT-GaAs substrate as a function of the bias voltage under an optical pump power of 720 mW. (b) Radiated terahertz power levels of the nanocavity-based terahertz source and the terahertz source fabricated on the LT-GaAs substrate as a function of the optical pump power under a bias voltage of 18 V.

Figure 2.16b shows the radiated terahertz power levels of the terahertz sources as a function of the optical pump power level under a bias voltage of 18 V. Higher enhancements in the optical-to-terahertz conversion efficiency are observed at lower optical pump powers compared with

those seen under stronger illumination. In fact, under an optical pump power of 10 mW, the nanocavity-based source produces terahertz radiation with an optical-to-terahertz conversion efficiency that is 62 times higher than that of the source fabricated on the LT-GaAs substrate, whereas this ratio decreases to 21 at an optical pump power of 720 mW. This reduction can again be attributed to the carrier screening and scattering induced by the high carrier concentration in the nanocavity at high optical pump power levels. These effects could be reduced by fabricating a larger area device and using an optical pump beam with a larger spot size.

The radiation fields from the terahertz sources are characterized using a time-domain terahertz spectroscopy system. The electro-optic detection method is applied using a 0.5 mm thick ZnTe crystal. An optical pump power of 720 mW and a bias voltage of 18 V are applied to both terahertz sources. Terahertz radiation is focused onto the electro-optic crystal using polyethylene terahertz lenses. Figure 2.17a shows the measured radiation fields from both sources. Pulses with a full width at half maximum of 0.45 ps are observed from both devices. The nanocavity-based terahertz source offers a peak-to-peak field that is 3.7 times stronger than that of the terahertz source fabricated on the LT-GaAs substrate. The radiation power spectra are calculated by taking the fast Fourier transforms of the radiation fields (Figure 2.17b). The nanocavity-based terahertz source offers 10 dB higher terahertz radiation power levels than the source fabricated on the LT-GaAs substrate for frequencies below 2 THz. This can again be attributed to the tighter light confinement near the plasmonic nanoantenna arrays and the higher carrier drift velocity offered by the low-defect semiconductor used in the nanocavity-based source. Similar radiation power levels are observed at frequencies above 2 THz. Only carriers generated within a few tens of nanometers distance from the nanoantennas can contribute to these high frequencies, and the carriers in this region are mostly generated via optical transmission by means of surface plasmon

waves. Since the plasmonic nanoantennas in both sources offer similar levels of optical absorption enhancement in this region, the radiation power levels at frequencies above 2 THz are expected to be similar. Radiation is observed throughout a broad frequency range extending up to 4 THz from both sources.

(a)

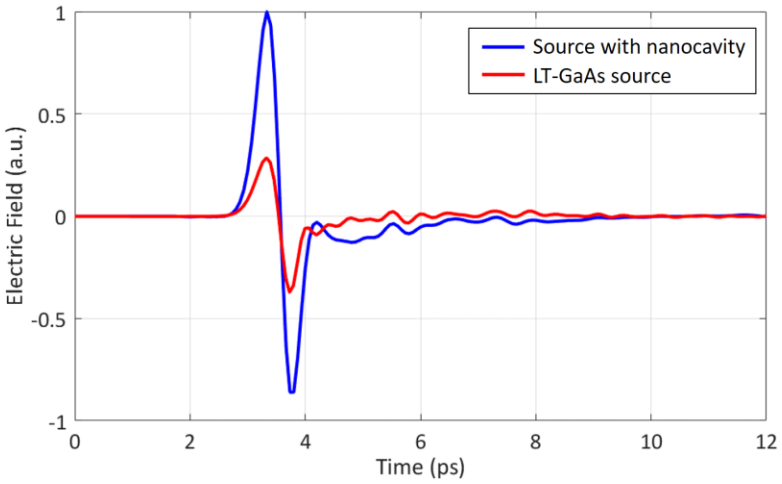

(b)

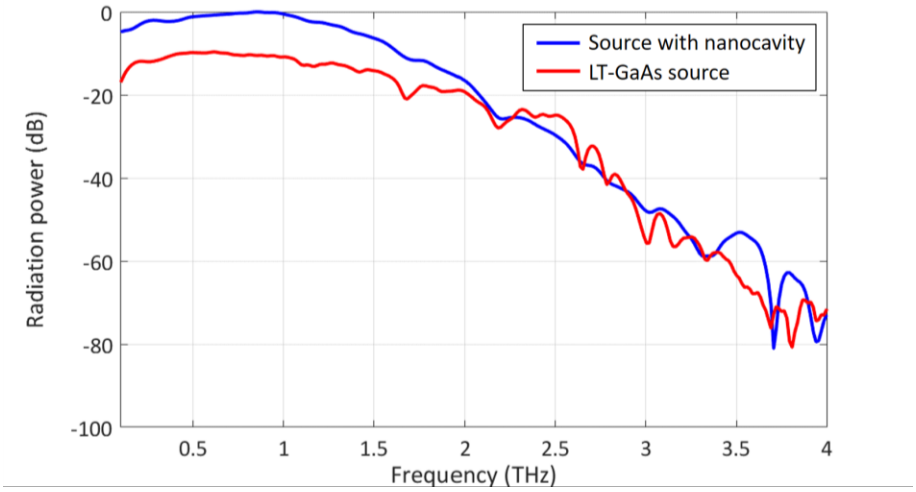

Figure 2.17. (a) The radiated electric fields and (b) the corresponding radiated power spectra of the nanocavity-based terahertz source and the terahertz source fabricated on the LT-GaAs substrate.

In summary, by enabling a much more efficient light confinement near the terahertz radiating elements and benefiting from higher carrier drift velocities offered by low-defect semiconductors, the nanocavity-based photoconductive terahertz source generates much stronger terahertz radiation compared with other source prototypes based on short-carrier-lifetime substrates. Using the nanocavity-based photoconductive terahertz source, a record-high power of 4 mW for pulsed terahertz radiation is achieved at an optical pump power of 720 mW over the 0.1-4 THz frequency range. This represents more than one order of magnitude enhancement in the optical-to-terahertz conversion efficiency compared with nanoantenna arrays fabricated on short-carrier-lifetime substrates. The nanocavity-based source also minimizes the thermal dissipation due to the slow carriers. Therefore, it offers a more reliable performance compared to SI-GaAs sources. Such a high-power, broadband, and high-reliability terahertz source could significantly improve the performance of future time-domain terahertz imaging and spectroscopy systems.

2.5. Telecommunication-Compatible Sources

Telecommunication wavelengths (e.g. 1550 nm) are one of the most desired regimes for pumping photoconductive sources due to availability of high-performance, low-cost and compact fiber lasers [64, 65]. However, performance of previously demonstrated photoconductive terahertz sources operating at telecommunication wavelengths has been limited by low resistivity of photo-absorbing semiconductor substrates at these wavelengths (e.g. InGaAs). This is because efficient operation of photoconductive terahertz sources requires accelerating photo-generated carriers by high bias electric fields, which results in high dark currents and thermal breakdown when using low resistivity substrates.

2.5.1. Source Design

Various techniques have been proposed to overcome the low resistivity limitation of photo-absorbing substrates at telecommunication wavelengths [66, 67]. One of the most promising solutions is use of a superlattice of monolayers of ErAs in an InGaAs substrate. Since the ErAs layers act as deep recombination centers inside ErAs:InGaAs superlattice, the resistivity and carrier lifetime of such superlattice structures can be controlled by the number and thickness of ErAs layers [68-71]. Although the high resistivity and short carrier lifetime characteristics of ErAs:InGaAs substrates can enable a more reliable device operation at telecommunication wavelengths, radiation power of previously demonstrated ErAs:InGaAs photoconductive terahertz sources operating at 1550 nm pump wavelengths has been limited by low quantum efficiency of conventional ultrafast photoconductors.

Therefore, a large-area photoconductive terahertz source based on a two-dimensional array of plasmonic nanoantennas is fabricated on an ErAs:InGaAs substrate to increase the optical-to-terahertz conversion efficiency.

Schematic diagram and operation concept of the ErAs:InGaAs photoconductive nanoantenna array is shown in Figure 2.18. It is fabricated on a 1 μm-thick ErAs:InGaAs layer, epitaxially grown on an InP substrate, with a carrier lifetime of 1.24 ps. A two-dimensional array of plasmonic nanoantennas is connected to anode bias lines within every other gap between the anode and cathode bias lines. The other gaps between the anode and cathode bias lines are shadowed by a second metal layer deposited on top of a Si_3N_4 antireflection coating. Geometry of the plasmonic nanoantennas, which are in the form of Au gratings, is chosen to excite surface plasmon waves when illuminated by the optical pump beam. To maintain high optical-to-

terahertz conversion efficiencies over broad bandwidths, the length of the nanoantennas is chosen as 5 μm.

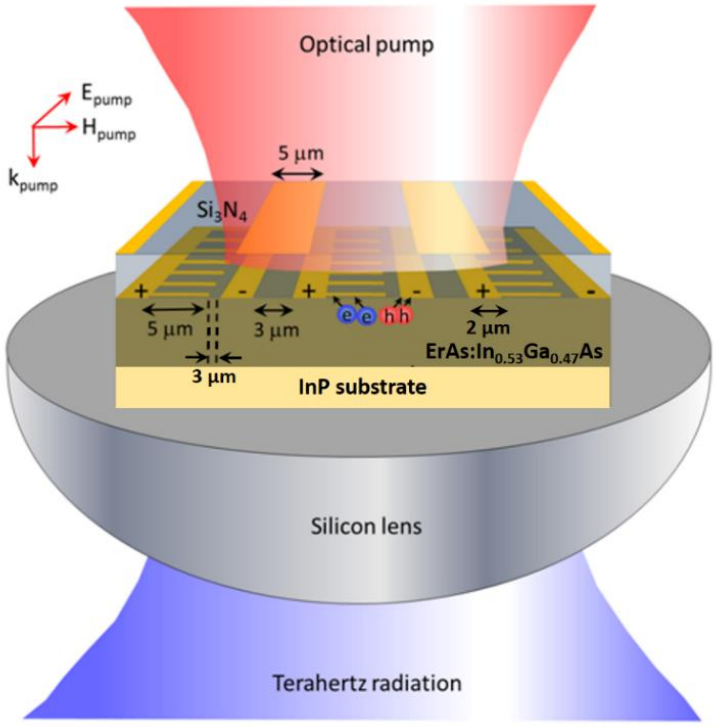

Figure 2.18. Schematic diagram of the presented photoconductive terahertz source based on a large-area plasmonic nanoantenna array fabricated on an ErAs:InGaAs substrate.

A Finite Element Method-based multi-physics solver (COMSOL) is used to analyze the interaction between the plasmonic nanoantennas and a TM-polarized optical pump beam. The analysis shows that use of Au nanoantennas with 50 nm height, 90 nm width, and 180 nm periodicity and a 250 nm Si_3N_4 antireflection coating layer offers 96% optical transmission into the ErAs:InGaAs substrate at 1550 nm pump wavelength (Figure 2.19). Since optical transmission into the substrate is accompanied by excitation of surface plasmon waves, optical absorption is significantly enhanced at the edges of the plasmonic nanoantennas (Figure 2.19 inset).

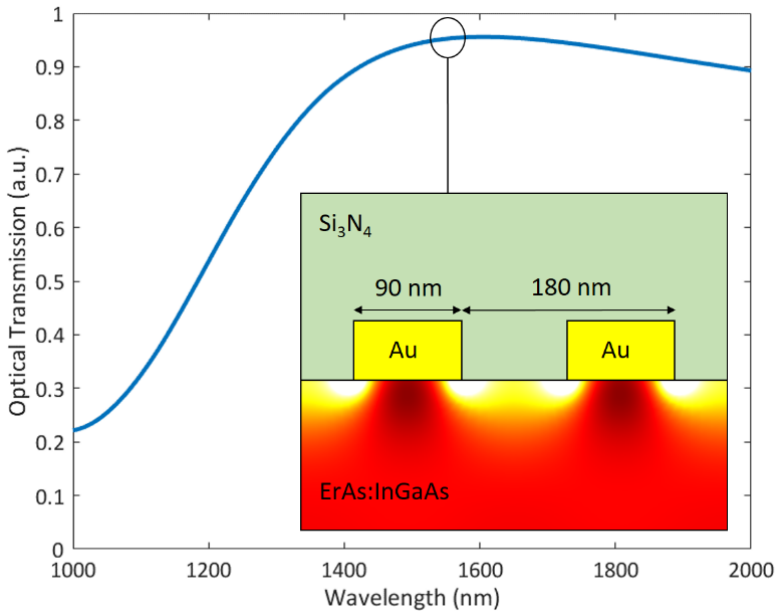

Figure 2.19. Optical transmission spectrum through the plasmonic nanoantennas into the ErAs:InGaAs substrate, inset shows optical absorption inside the ErAs:InGaAs substrate at 1550 nm pump wavelength.

2.5.2. Source Fabrication and Characterization

Prototypes of the presented plasmonic terahertz source with 0.5 × 0.5 mm^2 active area are fabricated on an ErAs:InGaAs substrate. The plasmonic nanoantennas are patterned by electron-beam lithography followed by 5/45 nm Ti/Au deposition and liftoff. The interdigitated bias lines are patterend by optical lithography followed by 40/360 nm Ti/Au deposition and liftoff. A 250 nm-thick Si_3N_4 antireflection coating layer is deposited next by plasma-enhanced chemical vapor deposition. After this step, shadow metals are patterned by optical lithography followed by 10/90 nm Ti/Au deposition and liftoff. Contact vias are patterned by optical lithography and opened by reactive ion etching of the Si_3N_4 layer. Optical microscope image of the device and scanning

electron microscope image (SEM) of the plasmonic nanoantennas are shown in Figures 2.20a and 2.20b, respectively.

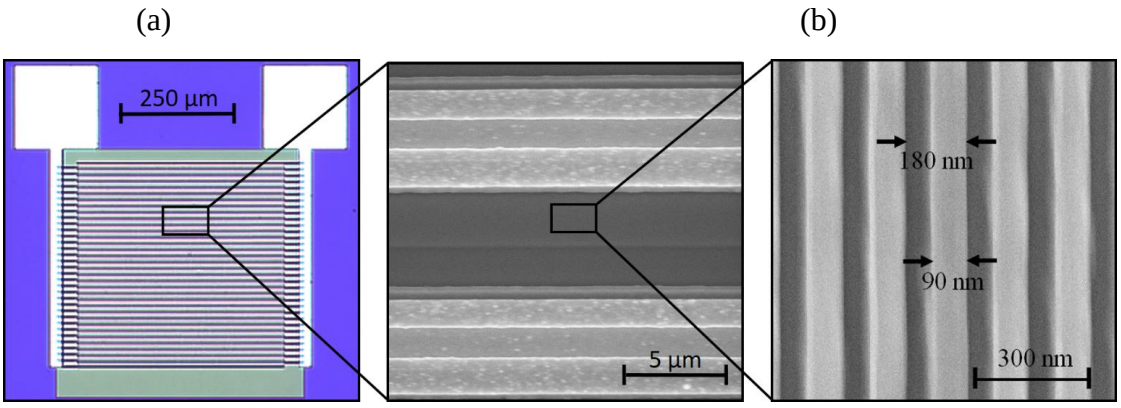

Figure 2.20. Optical microscope image of the plasmonic terahertz source and scanning electron microscope image of the plasmonic nanoantennas are shown in (a) and (b), respectively.

The fabricated terahertz sources are mounted on semi-hemispherical Si lenses and characterized in response to 1550 nm optical pump pulses with 170 fs width and 76 MHz repetition rate, generated by an optical parameter oscillator (OPO) pumped by a Ti:Sapphire laser. The optical pump spot size is adjusted to illuminate the entire device active area and its polarization is set to be normal to the plasmonic nanoantennas.

Figure 2.21a shows the induced photocurrent in a fabricated source prototype as a function of the optical pump power and bias voltage. The observed asymmetry in the photocurrent characteristics is due to the asymmetry in the photoconductor contact electrode areas as well as the higher drift velocities of photo-generated electrons compared to photo-generated holes under the same bias electric fields. A calibrated pyroelectric detector (Spectrum Detector, Inc. SPI-A-65 THz) is used to measure the radiated terahertz power from the source prototype [57]. Figure 2.21b shows the radiated terahertz power from the source prototype as a function of bias voltage and optical pump power. A non-quadratic relation between the radiated power and optical pump

power is observed, indicating that the source efficiency is degraded by the carrier screening effect. The impact of the carrier screening effect is more dominant at higher optical pump powers, since a larger number of photo-generated electrons and holes is separated from each other by the bias electric field. The negative impact of the carrier screening effect can be easily mitigated by using larger area plasmonic nanoantenna arrays. Terahertz radiation powers as high as 300 μW are achieved at 400 mW optical pump power, exhibiting the highest-reported terahertz radiation power from photoconductive terahertz sources operating at telecommunication wavelengths.

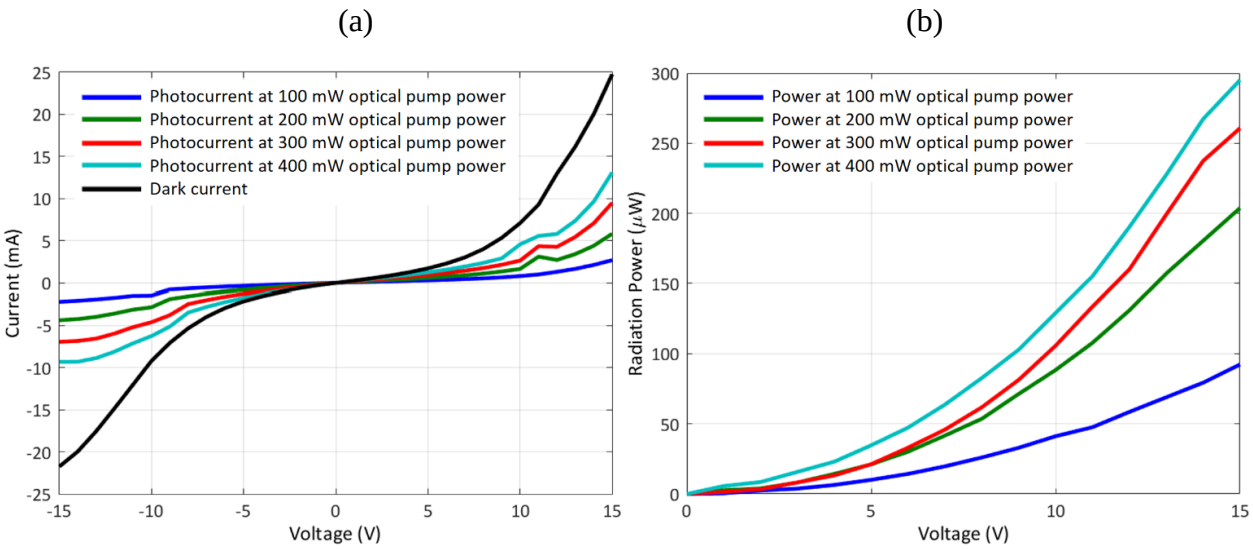

Figure 2.21. (a) The induced photocurrent and (b) terahertz radiation power from a large area plasmonic photoconductive source prototype as a function of the optical pump power and bias voltage.

A time-domain terahertz spectroscopy setup is used to measure the radiated electric field from the source prototype (Figure 2.22a). For this purpose, the 1550 nm optical beam from the OPO is split into two beams. One beam is used to pump the source prototype to generate terahertz

radiation. The other beam is focused onto a 0.6 mm-thick GaAs (110) crystal for electro-optic detection of the generated terahertz radiation. The bias voltage of the terahertz source is modulated between +15 and -15 V with a 3 kHz modulation frequency. Figure 2.22b shows the radiated electric field in the time domain at an optical pump power of 300 mW with a radiation pulse width of ~0.7 ps FWHM. Radiation spectrum is obtained from the Fourier transform of the measured radiated electric field. Figure 5c shows the calculated radiation spectrum, indicating radiation bandwidths of more than 5 THz and signal-to-noise ratio levels of 80 dB.

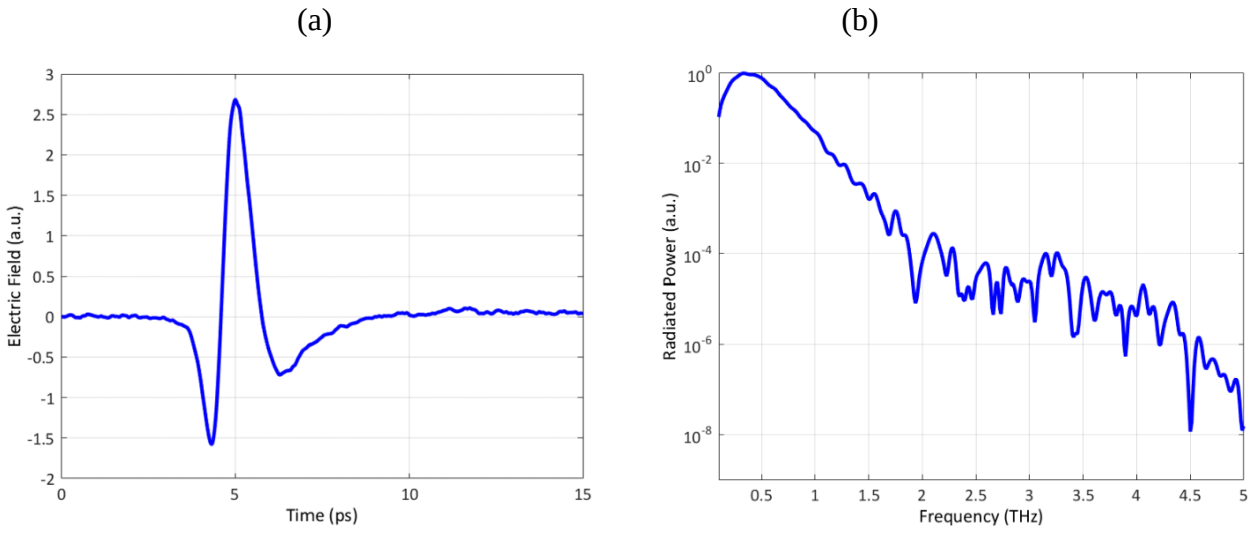

Figure 2.22. The radiated electric field in the time domain and radiated power in the frequency domain are shown in (a) and (b), respectively.

Although record-high terahertz radiation powers are offered by the large-area plasmonic nanoantenna arrays fabricated on ErAs:InGaAs at telecommunication wavelengths, the large-area plasmonic nanoantenna arrays fabricated on GaAs and pumped at 770-800 nm wavelengths offer much higher optical-to-terahertz conversion efficiencies and terahertz radiation powers. This can be attributed to the physical limitations of the available photo-absorbing semiconductors at 1550 nm wavelength. Although the ErAs:InGaAs superlattice offers higher

resistivity and shorter carrier lifetime compared with InGaAs, its resistivity is still much lower than the GaAs resistivity. The use of plasmonic nanocavities or higher-resistivity photo-absorbing semiconductor substrates at 1550 nm wavelength can certainly enhance the efficiency of these sources. For example, the material shown in Ref. [67] can be a very promising material for large-area plasmonic nanoantenna array terahertz sources operating at telecommunication wavelengths.

Chapter 3: Terahertz Detection through Large-Area Plasmonic Nanoantenna Arrays

3.1. Overview

Plasmonics-enhanced photoconductive antennas have shown great promise for increasing responsivity and detection sensitivity of conventional photoconductive detectors in time-domain terahertz imaging and spectroscopy systems. However, operation bandwidth of previously demonstrated plasmonic photoconductive antennas has been limited by bandwidth constraints of their antennas and photoconductor parasitics [40, 49]. To maintain broad operation bandwidths, previously demonstrated plasmonic photoconductive antennas have been realized with very small active areas to minimize capacitive loading to their terahertz antennas. This imposes very tight constraints on optical alignment and focusing for achieving acceptable detection sensitivities. This work presents large-area plasmonic photoconductive nanoantenna arrays as a powerful solution for addressing the limitations of previously demonstrated plasmonic photoconductive antennas used in terahertz time-domain spectroscopy systems. A key novelty that makes the presented terahertz detector superior to the state-of-the art is a specific device geometry that offers a strong interaction between an incident optical pump and terahertz beam at the nanoscale across a large device active area, while maintaining a broad operation bandwidth. The large device active area allows robust operation against optical and terahertz beam misalignments.

3.2. Detector Design

Schematic diagram and operation principles of plasmonic photoconductive nanoantenna arrays for detecting terahertz pulses are illustrated in Figure 3.1.

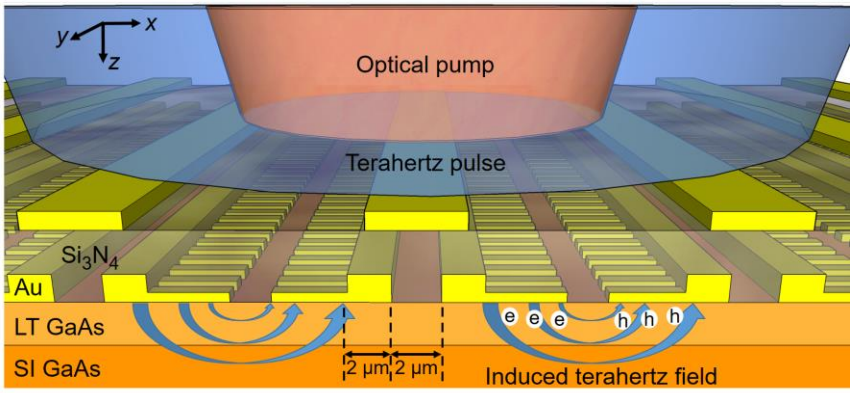

Figure 3.1. Schematic diagram of plasmonic photoconductive nanoantenna arrays used for detecting pulsed terahertz radiation.

The device consists of a two-dimensional array of plasmonic photoconductive nanoantennas fabricated on a short carrier lifetime substrate. The nanoantenna array size can be chosen arbitrarily large to facilitate coupling of the optical pump beam and terahertz radiation without strict alignment and focusing requirements. Dipole nanoantennas and low-temperature grown (LT) GaAs are used as the nanoantennas and short carrier lifetime substrate for the specific implementation discussed in this paper. The nanoantennas are connected in the vertical direction (along *y* axis) and separated from each other in the horizontal direction (along *x* axis), as illustrated in Figure 3.1. They are designed to offer a strong interaction between the incident terahertz and optical pump beams inside the device active area. For this purpose, the nanoantenna geometry is chosen to enhance the induced terahertz field between the nanoantenna tips when illuminated with an *x*-polarized terahertz beam. In the meantime, the length of the

nanoantennas is chosen to be much smaller than terahertz wavelengths to achieve broadband operation. The nanoantenna geometry is also chosen to allow excitation of surface plasmon waves when illuminated with a *y*-polarized optical pump beam. This concentrates majority of the photo-generated carriers in close proximity to the nanoantennas. Additionally, a Si_3N_4 antireflection coating layer is used to maximize optical transmission into the photo-absorbing substrate and an array of Au stripes on top of the Si_3N_4 layer is used to shadow the horizontal gaps between the nanoantennas. This prevents inducing a photocurrent in the opposite direction to that of the plasmonic photoconductive nanoantenna arrays. By significantly reducing the distance of majority of the photo-generated carriers from the nanoantennas and enhancing the induced terahertz field that drifts the photo-generated carriers, significantly higher responsivity and detection sensitivity levels can be achieved.

A Finite Element Method-based multi-physics software package (COMSOL) is used to analyze the interaction between the designed plasmonic nanoantennas, an *x*-polarized terahertz beam and a *y*-polarized optical beam. The analysis shows that Au gratings with 220 nm periodicity, 120 nm width, and 50 nm height, covered by a 290 nm thick Si_3N_4 antireflection coating layer offer 84% optical transmission into the LT-GaAs substrate at 800 nm wavelength (Figure 3.2a). Since optical transmission into the substrate is accompanied by excitation of surface plasmon waves, optical absorption is significantly enhanced at the edges of the plasmonic nanoantennas (Figure 3.2a inset). This enhancement factor is independent of the nanoantenna tip-to-tip gap size since the surface plasmon waves are excited by a *y*-polarized optical pump beam (Figure 3.2b). However, the nanoantenna tip-to-tip gap size directly impacts the optical absorption between the nanoantenna tips. While optical absorption between the nanoantenna tips is diffraction limited

for a nanoantenna tip-to-tip gap size of 250 nm, it is significantly increased when the tip-to-tip gap size is increased to 500 nm and 1 μm (Figure 3.2b inset).

(a)

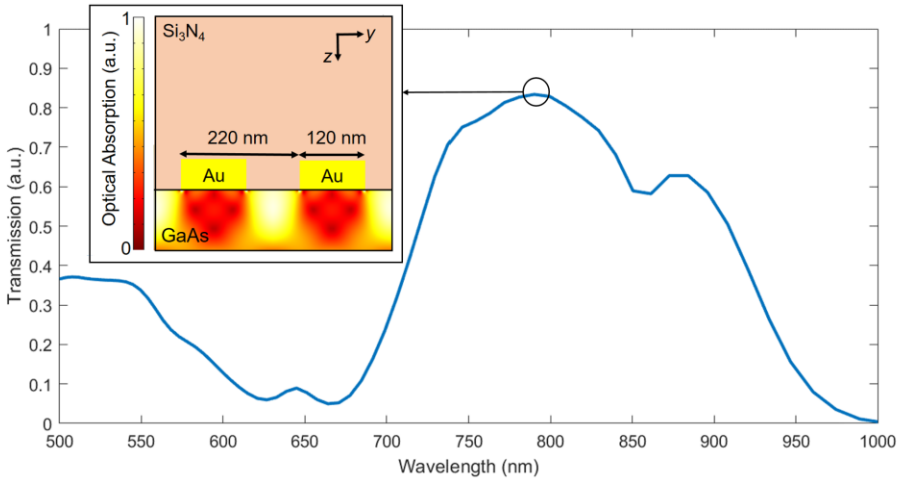

(b)

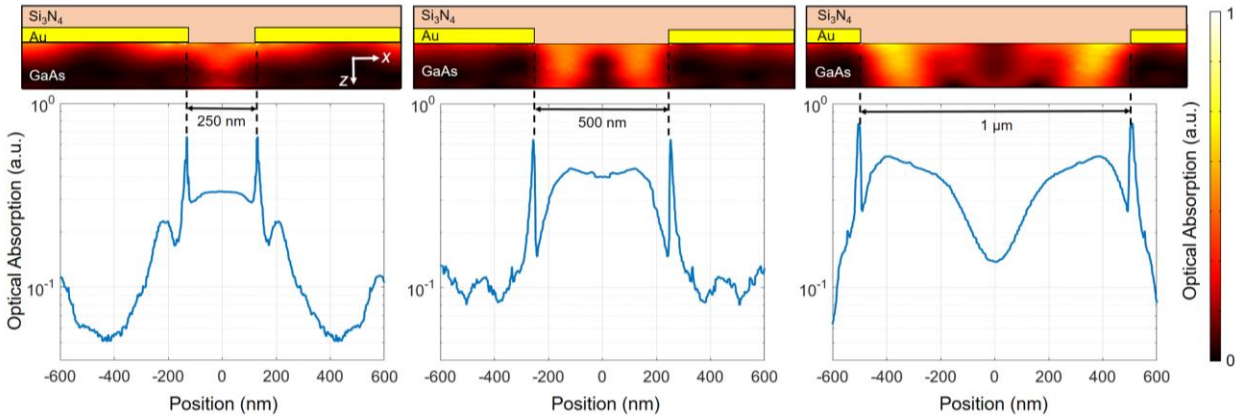

Figure 3.2. (a) Optical transmission spectrum through the plasmonic nanoantennas, inset shows optical absorption inside the substrate at a vertical cross-section of the nanoantennas at 800 nm pump wavelength. (b) Optical absorption between the nanoantenna tips at a 10 nm depth inside the substrate, the inset color plots show optical absorption profile within a 150 nm depth inside the substrate.

The length of the nanoantennas has a direct impact on the device operation bandwidth as well as terahertz field enhancement inside the device active area. Since the vertical gap size between the adjacent nanoantennas (220 nm) is much smaller than terahertz wavelengths, an *x*-polarized terahertz beam cannot transmit through the nanoantenna arms. It can efficiently transmit through the tip-to-tip gaps between the nanoantennas if $\lambda^{THz}{}_{eff} > \sqrt{\varepsilon_{r-sub}}\Lambda_x$, where $\lambda^{THz}{}_{eff}$ represents the effective wavelength of the incident terahertz beam inside the substrate, $\varepsilon_{r\text{-}sub}$ represents the relative permittivity of the substrate, and Λ_x represents the nanoantenna periodicity along the *x*-axis [55]. Under these circumstances, the induced terahertz field between the nanoantenna tips is proportional to Λ_x / g, where g represents the nanoantenna tip-to-tip gap size [55]. Therefore, higher terahertz field enhancement factors are offered by nanoantennas with smaller tip-to-tip gap sizes and larger lengths. The induced terahertz field is significantly reduced if $\lambda^{THz}{}_{eff} < \sqrt{\varepsilon_{r-sub}}\Lambda_x$. As a result, the device operation bandwidth is limited when using long nanoantennas [55].

Figure 3.3a shows the terahertz field enhancement factor in the middle of the nanoantenna tips as a function of frequency for different nanoantenna lengths. It illustrates the tradeoff between the field enhancement factor and operation bandwidth as a function of the nanoantenna length. While the field enhancement factor increases as the nanoantenna length increases from 2 μm to 7 μm, it starts to roll off above 5 THz for a nanoantenna length of 7 μm. Figure 3.3b shows the terahertz field enhancement factor in the middle of the nanoantenna tips as a function of frequency for different nanoantenna tip-to-tip gap sizes. As expected, the field enhancement factor is inversely proportional to the nanoantenna tip-to-tip gap size.

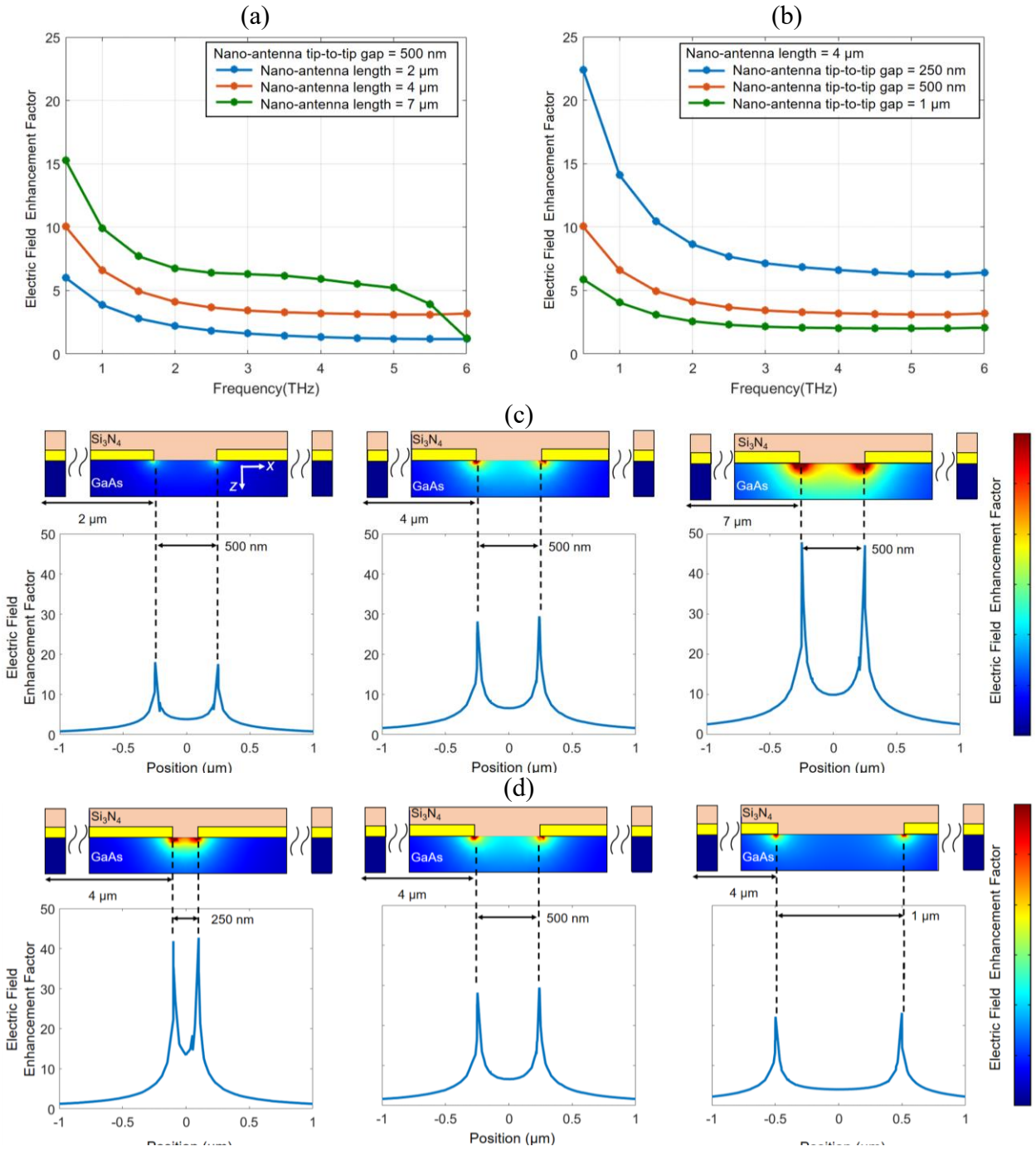

Figure 3.3. (a) Electric field enhancement factor in the middle of the nanoantenna tips as a function of the nanoantenna length and tip-to-tip gap size is shown in (a) and (b), respectively. Electric field enhancement factor between the nanoantenna tips at 1 THz as a function of the nanoantenna length and tip-to-tip gap size is shown in (c) and (d), respectively.

Since terahertz coupling is through excitation of surface waves along the nanoantenna arms, higher field enhancement factors are achieved in close proximity to the nanoantenna tips (Figs. 3c and 3d).

To achieve high-sensitivity terahertz detection, the nanoantenna geometry should be selected such that the induced terahertz field and optical pump intensity are maximized in close proximity to the nanoantenna tips. By maximizing the concentration of the photo-generated carriers and the electric field drifting the photo-generated carriers, higher photocurrent levels are induced in response to an incident terahertz beam and higher detection sensitivity levels are achieved, consequently. Therefore, designs with longer nanoantennas are preferred as far as the required detection bandwidths are supported by the device ($\lambda^{THz}{}_{eff} > \sqrt{\varepsilon_{r-sub}}\Lambda_x$). However, the optimum nanoantenna tip-to-tip gap size depends on different factors. On one hand, narrower tip-to-tip gaps offer stronger terahertz field enhancement factors inside the device active area. On the other hand, wider tip-to-tip gaps result in higher photocarrier concentration levels between the nanoantenna tips, where the highest terahertz field intensities are induced.

3.3. Detector Fabrication

To demonstrate the impact of the nanoantenna geometry on the device performance, terahertz detector prototypes with 0.5×0.5 mm^2 area, nanoantenna lengths of 2 μm and 4 μm, and nanoantenna tip-to-tip gap sizes of 250 nm, 500 nm, and 1 μm are fabricated on a LT-GaAs substrate (Figure 3.4). The fabrication process starts with patterning the plasmonic nanoantennas through electron beam lithography, followed by Au deposition and liftoff. The Au lines connecting the nanoantennas are patterned next by optical lithography, followed by metal deposition and liftoff. The Si_3N_4 antireflection coating layer is added next by using plasma-enhanced chemical vapor deposition. The shadow metals are also patterned by optical

lithography, followed by metal deposition and lift-off. Finally, contact vias are opened by reactive ion etching of the Si_3N_4 layer.

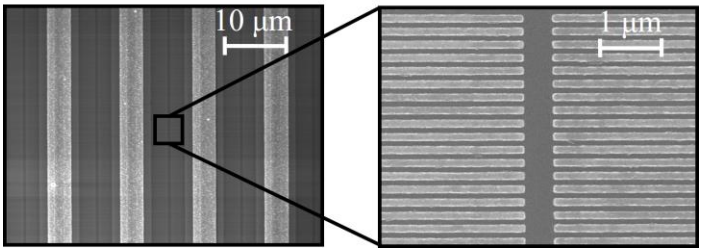

Figure 3.4. Scanning electron microscope image of a plasmonic nanoantenna array fabricated on a LT-GaAs substrate with a nanoantenna length of 2 μm and tip-to-tip gap size of 500 nm.

3.4. Detector Characterization

A time-domain terahertz spectroscopy setup is used to characterize performance of the fabricated detector prototypes under the same operation conditions. A LT-GaAs large-area plasmonic photoconductive terahertz source is used to generate terahertz pulses in the time-domain terahertz spectroscopy setup. 135 fs wide pulses from a Ti:sapphire mode-locked laser with 76 MHz repetition rate and 800 nm wavelength are used to pump the terahertz source and detector prototypes. The optical beam spot size is adjusted to 300 μm and its polarization is set to be normal to the nanoantennas. The polarization of the incident terahertz pulses on the detector prototypes is set to be parallel to the nanoantennas.

Figures 3.5a shows the measured photocurrent by a detector prototype with a nanoantenna length of 4 μm and tip-to-tip gap size of 500 nm in the time-domain. For each time-domain photocurrent data point, 35 measurements are taken and averaged with an integration time of 10 ms. Photocurrent pulses with 180 nA peak level and 0.45 ps FWHM width are measured at 200 mW optical pump power. Figure 3.5b shows the power spectra obtained from the time-domain

photocurrent data, indicating radiation detection bandwidths as high as 4.5 THz. A drop in the detector response is observed at optical pump powers exceeding 250 mW. This is due to the carrier screening effect caused by high photocarrier concentration levels at high pump powers.

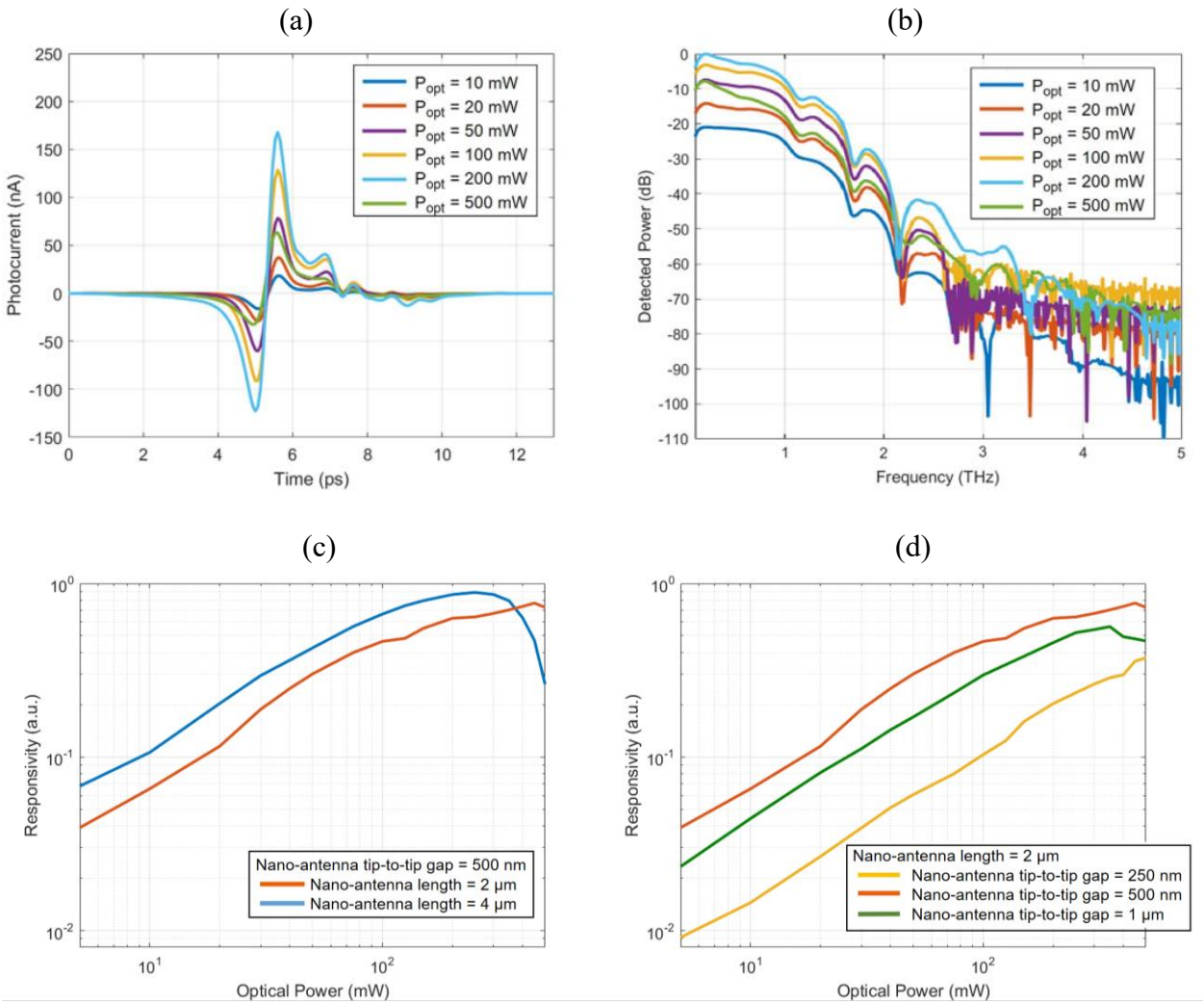

Figure 3.5. The measured photocurrent of a detector prototype with a nanoantenna length of 4 μm and tip-to-tip gap size of 500 nm in the time-domain and the corresponding power spectra are shown in (a) and (b), respectively. (c) Responsivity of detector prototypes with nanoantenna lengths of 2 μm and 4 μm and a tip-to-tip gap size of 500 nm at 1 THz, (d) responsivity of detector prototypes with a nanoantenna length of 2 μm and nanoantenna tip-to-tip gap sizes of 250 nm, 500 nm, and 1 μm at 1 THz.

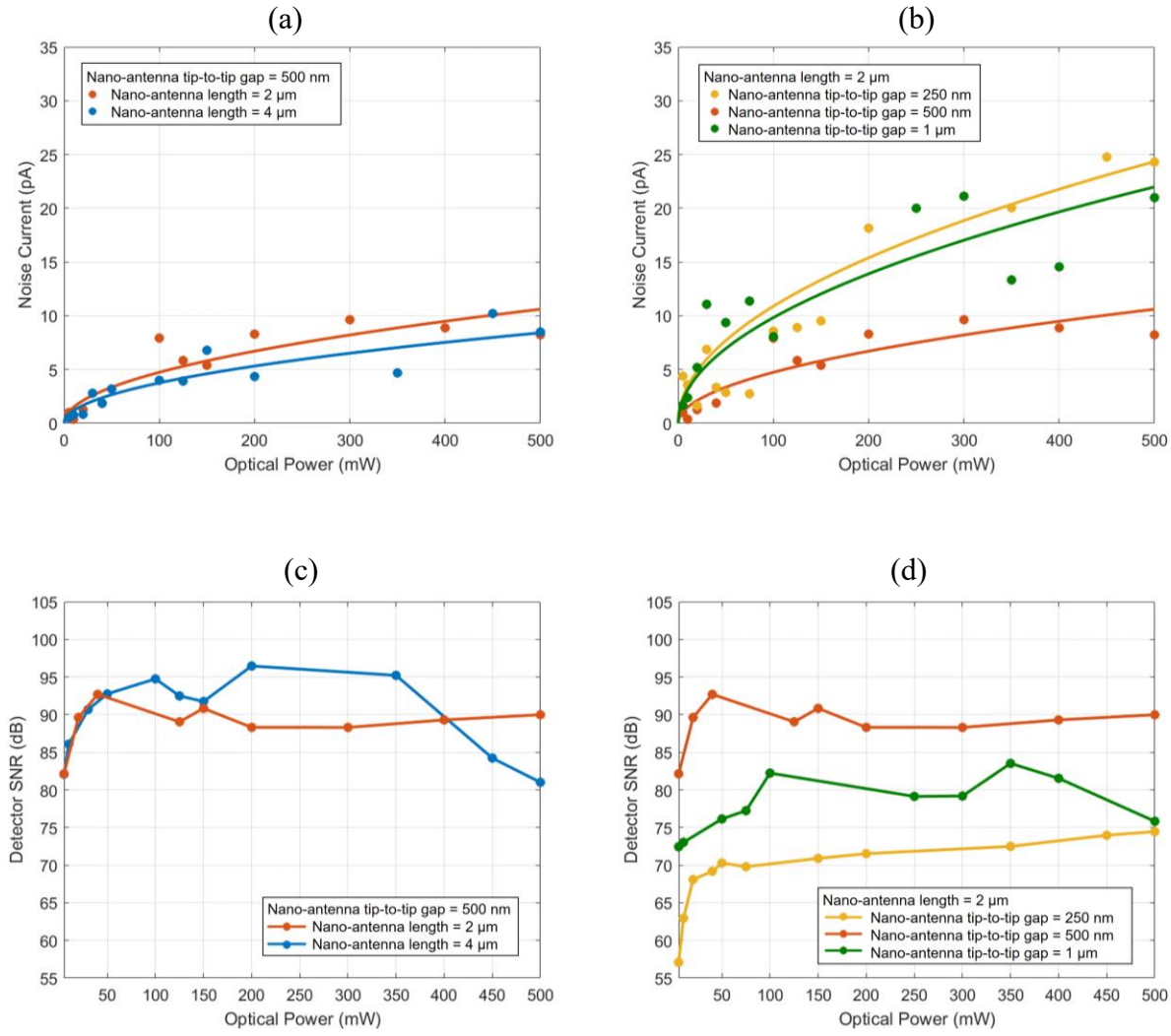

Figure 3.6. (a) The measured noise current of the detector prototypes with nanoantenna lengths of 2 μm and 4 μm and a tip-to-tip gap size of 500 nm, (b) the measured noise current of the detector prototypes with a nanoantenna length of 2 μm and nanoantenna tip-to-tip gap sizes of 250 nm, 500 nm, and 1 μm, (c) the measured SNR of the detector prototypes with nanoantenna lengths of 2 μm and 4 μm and a tip-to-tip gap size of 500 nm, (d) the measured SNR of the detector prototypes with a nanoantenna length of 2 μm and nanoantenna tip-to-tip gap sizes of 250 nm, 500 nm, and 1 μm.

Performance of devices with shorter nanoantennas is less affected by the carrier screening effect. This is because the number of the photo-generated carriers and the induced terahertz fields inside the device active area are smaller for devices with shorter nanoantennas. As illustrated in Figure 3.5c, while the responsivity of the detector prototype with a nanoantenna length of 4 μm and tip-to-tip gap size of 500 nm rolls off at optical pump powers above 250 mW, the responsivity of a similar detector prototype with a nanoantenna length of 2 μm does not show any drop up to 450 mW optical pump power. Despite the negative impact of the carrier screening effect, higher responsivity levels are offered by the detector with a nanoantenna length of 4 μm at optical pump powers below 350 mW. This is due to the larger number of photocarriers and higher terahertz field levels induced inside the device active area.

As discussed in previous sections, narrower nanoantenna tip-to-tip gaps offer stronger terahertz field enhancement factors but result in lower photocarrier concentration levels inside the device active area. This tradeoff can be clearly observed when comparing the responsivity of detector prototypes with the same nanoantenna length of 2 μm and tip-to-tip gap sizes of 250 nm, 500 nm, and 1 μm (Figure 3.5d). Although the highest terahertz field enhancement factors and photocarrier concentration levels are offered by the nanoantennas with tip-to-tip gap sizes of 250 nm and 1 μm, respectively, the highest responsivity levels are achieved by the nanoantenna with a tip-to-tip gap size of 500 nm. Moreover, the device with a nanoantenna tip-to-tip gap size of 250 nm is less affected by the carrier screening effect due to low photocarrier concentration levels inside the device active area.

The same time-domain terahertz spectroscopy system is used to measure noise characteristics of the detector prototypes. The optical beam pumping the terahertz source is blocked and the detector noise current is measured from the root mean square (rms) value of the induced

photocurrent. The measurement results show that the detector noise current does not have a considerable dependence on the nanoantenna length (Figure 3.6a), but has a strong dependence on the nanoantenna tip-to-tip gap size (Figure 3.6b). This is because the primary noise source for the presented plasmonic photoconductive detector is the Johnson-Nyquist noise [37, 38], with a noise current inversely proportional to the square root of the device resistance. Among the three detector prototypes with a nanoantenna length of 2 μm, the design with a nanoantenna tip-to-tip gap size of 500 nm offers the highest resistance and lowest noise current, consequently. Similarly, the design with a nanoantenna tip-to-tip gap size of 250 nm offers the lowest resistance and highest noise current. Since the device resistance is inversely proportional to the optical pump power level, a linear relation is observed between the noise current and the square root of the optical pump power.

Signal-to-noise ratio (SNR) of the detector prototypes is calculated from the measured photocurrent and noise current data. A relatively linear relation between the SNR and optical pump power is observed at optical pump power levels below 50 mW. This is because the detector responsivity is proportional to the optical pump power and the noise current is proportional to the square root of the optical pump power. Lower increase in SNR values is observed at higher optical pump power levels due to the carrier screening effect. The designs with longer nanoantennas (Figure 3.6c) and wider nanoantenna tip-to-tip gaps (Figure 3.6d), which are more susceptible to the carrier screening effect, exhibit a roll-off in their SNR values at optical pump powers exceeding 200 mW. The highest SNR values are offered by the detector prototype with a nanoantenna length of 4 μm and tip-to-tip gap size of 500 nm due to its superior responsivity and noise performance. The SNR values can be further improved by reducing noise current through increasing the number of data points and data acquisition times [65]. SNR values

as high as 107 dB over 5 THz frequency are offered by the detector prototype with a nanoantenna length of 4 μm and a tip-to-tip gap size of 500 nm at 170 mW optical pump power when capturing and averaging 750 photocurrent data points with an integration time of 10 ms (Figure 3.7). The SNR enhancement is mainly due to noise current reduction from 5 pA to 1.3 pA when increasing the data points from 35 to 750 [65]. This is the highest reported SNR level for a photoconductive terahertz detector, exhibiting 50 times enhancement compared to the state-of-the art [65]. Such high-performance terahertz detectors could extend scope and potential use of compact time-domain terahertz spectroscopy systems for many imaging and sensing applications.

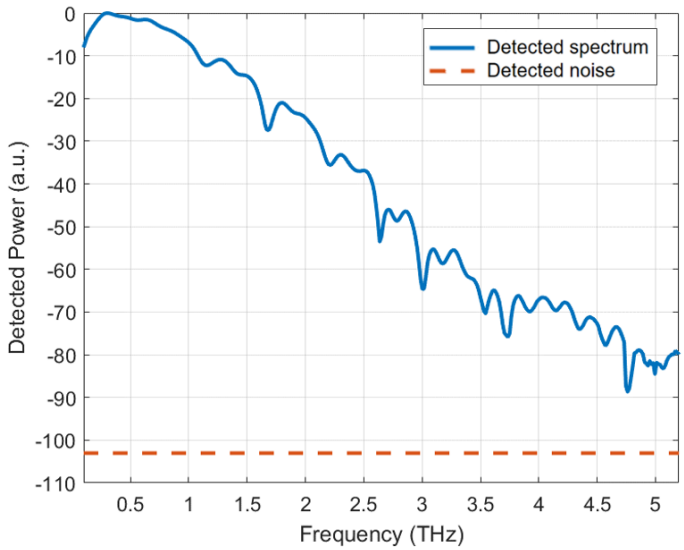

Figure 3.7. The measured power spectrum by the detector prototype with a nanoantenna length of 4 μm and a tip-to-tip gap size of 500 nm relative to the measured noise power at 170 mW optical pump power. The presented data are achieved by capturing and averaging 750 photocurrent data points with an integration time of 10 ms.

Chapter 4: Conclusion and Future Directions

The main goal of this dissertation is satisfying the need for high-power terahertz sources and high-sensitivity terahertz detectors operating over a broad terahertz frequency range to enhance the performance of time-domain terahertz imaging and spectroscopy systems. Novel photoconductive terahertz sources and detectors based on two-dimensional plasmonic nanoantenna arrays are designed, fabricated and characterized.

It is demonstrated that incorporating two-dimensional plasmonic nanoantenna arrays in large-area photoconductive sources enhances their optical-to-terahertz efficiency significantly. A thorough investigation of plasmonic nanoantenna arrays as terahertz sources is carried out and the effects of the nanoantenna geometry and semiconductor substrate characteristics are analyzed theoretically and experimentally. Furthermore, a higher-performance device architecture based on plasmonic nanocavities is presented, which offers high optical-to-terahertz conversion efficiency and robust performance with low thermal dissipation simultaneously. Pulsed terahertz generation with record-high powers as high as 4 mW over a 0.1-4 THz frequency range is achieved at a 770 nm optical pump wavelength. Moreover, a high-performance photoconductive source based on plasmonic nanoantenna arrays is designed to operate at telecommunication optical wavelengths. It is demonstrated that large-area plasmonic nanoantenna arrays fabricated on ErAs:InGaAs offer record-high terahertz radiation powers compared to the previously demonstrated terahertz sources operating at telecommunication pump wavelengths. However, the terahertz radiation power of these sources is much lower than large-area plasmonic nanoantenna arrays fabricated on GaAs and pumped at 770-800 nm wavelengths. This is due to the low resistivity of the available photo-absorbing semiconductors at 1550 nm wavelength. The use of

higher-resistivity photoconductive substrates and plasmonic nanocavities designed for three-dimensional light confinement at telecommunication optical wavelengths can address this limitation.

It is also demonstrated that incorporating two-dimensional plasmonic nanoantenna arrays in large-area photoconductive detectors enhances their responsivity and detection sensitivity significantly. A high-performance terahertz detector based on plasmonic photoconductive nanoantenna arrays is designed and characterized. The nanoantenna arrays are specifically designed to allow a strong interaction between the incident optical pump and terahertz beam across a large device active area and over a broad range of terahertz frequencies to enhance the detection sensitivity and bandwidth. The large device active area also allows robust operation without tight constraints on optical alignment and focusing. To find the optimum designs, the impact of the detector geometry on its responsivity and noise characteristics is analyzed numerically and experimentally. The use of plasmonic nanocavities could further enhance the responsivity and detection sensitivity of these terahertz detectors. By using these novel sources and detectors, terahertz detection over bandwidths exceeding 5 THz with record-high SNR levels as high as 107 dB is demonstrated. Such high-performance terahertz sources and detectors could extend the scope and potential use of compact time-domain terahertz spectroscopy systems for many imaging and sensing applications.

References

[1] M. Tonouchi, “Cutting-edge terahertz technology,” Nature Photonics, vol. 1, pp. 97-105, 2007.

[2] D. G. Rowe, “Terahertz takes to the stage,” Nature Photonics, vol. 1, pp. 75-77, Feb. 2007.

[3] P. H, Siegel, “Terahertz Technology,” IEEE Trans. Microw. Theory Techn., vol. 50, pp. 910-928, 2002.

[4] F. A. Miller, “Far infra-red spectroscopy,” in Molecular Spectroscopy. The Institute of Petroleum,

1968, pp. 5–27.

[5] A. Menikh, S. P. Mickan, H. Liu, R. MacColl, X.-C. Zhang, “Label-free amplified bioaffinity detection using terahertz wave technology,” Biosens. Bioelectron., vol. 20, pp. 658-662, 2004.

[6] Y. C. Shen et. al., “Detection and identification of explosivies using terahertz pulsed spectroscopic imaging,” Appl. Phys. Lett., vol. 86, pp. 86-88, 2005.

[7] M. Naftaly, R. E. Miles, “Terahertz time-domain spectroscopy for material characterization,” Proc. IEEE, vol. 95, pp. 1658-1665, 2007.

[8] R. M. Woodward et. al., “Terahertz pulse imaging in reflection geometry of human skin cancer and skin tissue,” Phys. Med. Biol., vol. 47, pp. 3853-3863, 2002.

[9] C. D. Stoik, M. J. Bohn, J. L. Blackshire, “Nondestructive evaluation of aircraft composites using transmissiove terahertz time domain spectroscopy,” Opt. Express, vol. 16, pp. 17039-17051, 2008.

[10] W. R. Tribe, D. A. Newnham, P. F. Taday, M. C. Kemp, “Hidden object detection: security applications of terahertz technology,” in Integrated Optoelectronic Devices 2004 (pp. 168-176).

[11] N. Karpowicz, “Comparison between pulsed terahertz time-domain imaging and continuous wave terahertz imaging,” Semicond. Sci. Technol., vol. 20, pp. 293-299, 2005.

[12] S. Preu, G. H. Döhler, S. Malzer, L. J. Wang, A. C. Gossard, “Tunable, continuous-wave terahertz photomixer sources and applications,” J. Appl. Phys., vol. 109, pp. 061301, 2011.

[13] B. M. Fischer, M. Walther, P. U. Jepsen, ”Far-infrared vibrational modes of DNA components studied by terahertz time-domain spectroscopy,” Phys. Med. Biol., vol. 47, pp. 3807, 2002.

[14] A. A. Gowen, C. O’Sullivan, C. P. O’Donnell, “Terahertz time domain spectroscopy and imaging: Emerging techniques for food process monitoring and quality control,” vol. 25, pp. 40-46, 2012.

[15] M. Scheller, C. Jansen, M. Koch, “Analyzing sub-100-μm samples woth transmission terahertz timedomain spectroscopy,” Opt. Commun, vol. 282, pp. 1304-1306, 2009.

[16] Y.-S. Lee, T. Meade, V. Perlin, H. Winful, T. B. Norris, “Generation of narrow-band terahertz radiation via optical rectification of femtosecond pulses in periodically poled lithium niobate,” Appl. Phys. Lett., vol. 76, pp. 2505, 2000.

[17] K. Ravi et. al.,”Theory of terahertz generation by optical rectification using tilted-pulse-front,” Opt. Express, vol. 23, pp. 5253-5276, 2015.

[18] P. N. Butcher and D. Cotter, “The Elements of Nonlinear Optics”, Cambridge University Press, Cambridge, U. K., 1990.

[19] K.-L. Yeh, M. C. Hoffmaa, J. Hebling, K. A. Nelson, “Generation of 10 μJ ultrashort terahertz pulses by optical rectification,” Appl. Phys. Lett., vol. 90, pp. 171121, 2007.

[20] D. H. Auston, K. P. Cheung, P. R. Smith, “Picosecond photocoducting Hertzian dipoles,” Appl. Phys. Lett., vol. 45, pp. 284–286, 1984.

[21] P. U. Jepsen, R. H. Jacobsen, S. R. Keiding, “Generation and detection of terahertz pulses from biased semiconductor antennas,” J. Opt. Soc. Am. B, vol. 13, pp. 2424, 1996.

[22] T.-C. Shen, P. C. Upadhya, E. H. Linfield, H. E. Beere, A. G. Davies, “Ultrabroadband terahertz radiation from low-temperature-grown GaAs photoconductive emitters,” Appl. Phys. Lett., vol. 83, pp. 3117–3119, 2003.

[23] M. Tani, S. Matsuura, K. Sakai, S. Nakashima, “Emission characteristics of photoconductive antennas based on low-temperature-grown GaAs and semi-insulating GaAs,” Appl. Opt., vol. 36, pp. 7853-7859, 1997.

[24] W. L. Barnes, A. Dereux, T. W. Ebbesen, “Surface plasmon subwavelength optics,” Nature, vol. 424, pp. 824-830, 2003.

[25] M. Beck, H. Schäfer, G. Klatt, J. Demsar, S. Winnerl, M. Helm, T. Dekorsy, “Impulsive terahertz radiation with high electric fields from an amplifier-driven large-area photoconductive antenna,” Opt. Express, vol. 18, pp. 9251-9257, Apr. 2010.

[26] A. Dreyhaupt, S. Winnerl, T. Dekorsy, and M. Helm, "High-intensity terahertz radiation from a microstructured large-area photoconductor," Appl. Phys. Lett., vol.86, p. 121114, 2005.

[27] S. Winnerl, “Scalable Microstructured Photoconductive Terahertz Emitters,” J. Infrared. Milim.. Teahz Waves, vol. 33, pp. 431-454, 2012.

[28] Q. Wu, X.-C. Zhang, “Free-space electro-optic sampling of terahertz beams,” Appl. Phys. Lett., vol. 67, pp. 3523, 1995.

[29] G. Gallot, D. Grischkowsky, “Electro-Optic Detection of Terahertz Radiation,” J. Opt. Soc. Am. B., vol. 16, pp. 1204-1212, 1999.

[30] Q. Wu and X. C. Zhang, “7 Terahertz Broadband GaP Electro-Optic Sensor," Appl.Phys. Lett., vol. 70, pp. 1784-1786, 1997.

[31] Q. Wu, M. Litz, X.-C. Zhang, "Broadband detection capability of ZnTe electro-optic field detectors," Appl. Phys. Lett., vol. 68, pp. 2924, 1996.

[32] G. Gallot, Jiangquan Zhang, R. W. McGowan, Tae-In Jeon, and D. Grischkowsky, "Measurements of the THz absorption and dispersion of ZnTe and their relevance to the electro-optic detection of THz radiation," Appl. Phys. Lett., vol. 74, pp. 3450, 1990.

[33] Z. Zhao et. al., "Thickness dependence of the terahertz response in <110>-oriented GaAs crystals for electro-optic sampling at 1.55 μm," Opt. Express, vol. 18, pp. 15956-15963, 2010.

[34] S., Kono, M. Tani, P. Gu, K Sakai, "Detection of up to 20 THz with Low-Temperature-Grown GaAs Photoconductive Antenna Gate with 15 fs Light Pulses," Appl. Phys. Lett., vol. 77, pp. 4104-4106, 2000.

[35] F. J. O'Hara, J. M. O. Zide, A. C. Gossard, A. J. Taylor, R. D. Averitt, "Enhanced Terahertz Detection via ErAs:GaAs Nanoisland Superlattices." Appl. Phys. Lett., vol. 88, pp. 251119-251121, 2006.

[36] K. Peng et al. "Single Nanowire Photoconductive Terahertz Detectors," Nanolett., vol. 15, pp. 206-210, 2015.

[37] N. Wang, M. Jarrahi, "Noise Analysis of photoconductive terahertz detectors," J. Infrared Millim. Terahertz Waves, vol. 34, pp. 519-528, 2013.

[38] E. Castro-Camus, L. Fu, J. Lloyd-Hughes, H. H. Tan, C. Jagadish, M. B. Johnston, "Photoconductive Response Correction for Detectors of Terahertz Radiation," J. Appl. Phys., vol.104, pp.053113, 2008.

[39] C. W. Berry, M. Jarrahi, "Terahertz generation using plasmonic photoconductive gratings," New J. Phys., vol. 14, p. 105029, Oct. 2012.

[40] C. W. Berry, N. Wang, M. R. Hashemi, M. Unlu, M. Jarrahi, "Significant Performance Enhancement in Photoconductive Terahertz Optoelectronics by Incorporating Plasmonic Contact Electrodes," Nat. Commun., vol. 4, p. 1622, Mar. 2013.

[41] S. H. Yang, M. R. Hashemi, C. W. Berry, M. Jarrahi, "7.5% optical-to-terahertz conversion efficiency offered by photoconductive emittters with three-dimensional plasmonic contact electrodes," IEEE Trans. Terahertz Sci. Technol, vol. 4, pp. 575-581, Sep. 2014.

[42] C. W. Berry, M. R. Hashemi, S. Preu, H. Lu, A. C. Gossard, M. Jarrahi, "High Power Terahertz Generation Using 1550 nm Plasmonic Photomixers", Appl. Phys. Lett., vol. 105, p. 011121, 2014.

[43] C. W. Berry, M. R. Hashemi, M. Jarrahi, "Generation of High Power Pulsed Terahertz Radiation using a Plasmonic Photoconductive Emitter Array with Logarithmic Spiral Antennas", Appl. Phys. Lett., vol. 104, p. 081122, 2014.

[44] N. Wang, M. R. Hashemi, M. Jarrahi, "Plasmonic photoconductive detectors for enhanced terahertz detection sensitivity", Opt. Express, vol. 21, pp. 17221-17227, 2013.

[45] B. Heshmat, H. Pahlevaninezhad, Y. Pang, M. Masnadi-Shirazi, R. B. Lewis, T. Tiedje, R. Gordon, T. E. Darcie, “Nanoplasmonic Terahertz Photoconductive Switch on GaAs,” Nano Lett., vol. 12, pp. 6255-6259, Nov. 2012.

[46] S.-G. Park, K. H. Jin, M. Yi, J. C. Ye, J. Ahn, and K.-H. Jeong, “Enhancementof terahertz pulse emission by optical nanoantenna,” ACS Nano, vol. 6, pp. 2026–2031, Feb. 2012.

[47] S. Liu, X. Shou, A. Nahata, “Coherent Detection of Multiband Terahertz Radiation Using a Surface Plasmon-Polariton Based Photoconductive Antenna,” IEEE Trans. THz Sci. Technol., vol. 1, pp. 412-415, Nov. 2011.

[48] S.-G. Park, Y. Choi, Y.-J. Oh, K.-H. Jeong, “Terahertz photoconductive antenna with metal nanoislands,” Opt. Express, vol. 20, 25530, Nov. 2012.

[49] M. Jarrahi, "Advanced Photoconductive Terahertz Optoelectronics based on Nano-Antennas and Nano-Plasmonic Light Concentrators," IEEE Trans. THz Sci. Technol., vol. 5, pp. 391-397, 2015.

[50] N. T. Yardimci, S.-H. Yang, C. W. Berry, M. Jarrahi, "High Power Terahertz Generation Using Large Area Plasmonic Photoconductive Emitters," IEEE Trans. THz Sci. Technol., vol. 5, pp. 223-229, 2015.

[51] N. T. Yardimci, R. Salas, Erica M. Krivoy, Hari P. Nair, S. R. Bank, M. Jarrahi, "Impact of Substrate Characteristics on Performance of Large Area Plasmonic Photoconductive Emitters," Opt. Express, vol. 23, pp. 32035-32043, 2015.

[52] C. Genet, T. W. Ebbesen, “Light in tiny holes,” Nature, vol. 445, pp. 39-46, 2007.

[53] N. T. Yardimci, M. Jarrahi, "High power telecommunication-compatible photoconductive terahertz emitters based on plasmonic nano-antenna arrays," Applied Physics Letters, vol. 109, pp. 191103, 2016.

[54] N. T. Yardimci, M. Jarrahi, "High Sensitivity Terahertz Detection through Plasmonic Nano-Antenna Arrays," Sci. Rep., vol. 7, pp. 42667, 2017.

[55] B-Y. Hsieh, M. Jarrahi, “Analysis of periodic metallic nano-slits for efficient interaction of terahertz and optical waves at nano-scale dimensions,” J. Appl. Phys., vol. 109, pp. 084326, 2011.

[56] C. A. Balanis, Antenna Theory: Analysis and design, 3rd ed. (John Wiley & Sons, Hoboken, New Jersey, USA, 2005).

[57] C. W. Berry, N. T. Yardimci, M. Jarrahi, "Responsivity Calibration of Pyroelectric Terahertz Detectors", arXiv:1412.6878v1, 2014.

[58] C. W. Berry, M. Jarrahi, “Principles of impedance matching in photoconductive antennas,” J. Infrared Millim. THz Waves, vol. 33, pp. 1182–1189, 2012.

[59] H. Nemec, A. Pashkin, P. Kuzel, M. Khazan, S. Schnull, and I. Wilke, “Carrier dynamics in low temperature grown GaAs studied by terahertz emission spectroscopy,” J. Appl. Phys., vol 90, pp. 1303, 2001.

[60] M. Griebel, et. al, “Tunable subpicosecond optoelectronic transduction in superlattices of self-assembled ErAs nanoislands,” Nat. Mater., vol. 2, pp. 122–126, 2003.

[61] H. T. Chen, et. al., “Ultrafast optical switching of terahertz metamaterials fabricated on ErAs/GaAs nanoisland superlattices,” Opt. Lett., vol. 32, pp. 1620–1622, 2007.

[62] R. P. Prasankumar et. al., “Carrier dynamics in self-assembled ErAs nanoislands embedded in GaAs measured by optical-pump terahertz-probe spectroscopy,” Appl. Phys. Lett., vol. 86, pp. 201107 (2005).

[63] E. M. Krivoy, et. al. “Growth and characterization of LuAs films and nanostructures,” Appl. Phys. Lett., vol. 101, pp. 141910, 2012.

[64] B. Sartorius, et. al., “All-fiber terahertz time-domain spectrometer operating at 1.5 μm telecom wavelengths,” Opt. Express, vol. 16, pp. 9565-9570, 2008.

[65] N. Vieweg, et. al. “Terahertz-time domain spectrometer with 90 dB peak dynamic range,” J. Infrared Millim. Terahertz Waves, vol. 35, pp. 823-832, 2014.

[66] M. Suzuki, M. Tonouchi, “Fe-implanted InGaAs terahertz emitters for 1.56 μm wavelength excitation,” Appl.Phys. Lett., vol. 86, pp. 051104, 2005.

[67] H. Roehle, et. al., “Next generation 1.5 μm terahertz antennas: mesa-structuring of InGaAs/InAlAs photoconductive layers,” Opt. Express, vol. 18, pp. 2296-2301, 2010.

[68] A. K. Azad, et. al., “Carrier dynamics in InGaAs with embedded ErAs nanoislands,” Appl. Phys. Lett., vol. 93, pp. 121108, 2008.

[69] Schwagmann, et. al., “Terahertz emission characteristics of ErAs:InGaAs-based photoconductive antennas excited at 1.55 μm,” Appl. Phys. Lett., vol. 96, pp. 141108, 2010.

[70] M. Sukhotin, et. al., “Photomixing and photoconductor measurements on ErAs/InGaAs at 1.55 μm,” Appl. Phys. Lett., vol. 82, pp. 3116, 2003.

[71] S. Preu, et. al. “1550 nm ErAs:In(Al)GaAs large area photoconductive emitters,” Appl. Phys. Lett., vol. 101, pp. 101105, 2012.